Phonon-mediated strong coupling between a three-dimensional topological insulator and a two-dimensional antiferromagnetic material

D. Quang To, Weipeng Wu, Subhash Bhatt, Yongchen Liu, Anderson Janotti, Joshua M. O. Zide, Mark J. H. Ku, John Q. Xiao, M. Benjamin Jungfleisch, Stephanie Law, and Matthew F. Doty

Phonon-mediated strong coupling between a three-dimensional topological insulator and a two-dimensional antiferromagnetic material

D. Quang To,[1] Weipeng Wu,[2] Subhash Bhatt,[2] Yongchen Liu,[1] Anderson Janotti,[1] Joshua M.O. Zide,[1] Mark J.H. Ku,[1,2] John Q. Xiao,[2] M. Benjamin Jungfleisch,[2] Stephanie Law,[1,*] and Matthew F. Doty[1,†]

[1]*Department of Materials Science and Engineering, University of Delaware, Newark, DE 19716, USA*
[2]*Department of Physics and Astronomy, University of Delaware, Newark, DE 19716, USA*
(Dated: March 3, 2023)

We numerically study strong coupling between THz excitations in a hybrid material consisting of a three dimensional (3D) topological insulator (TI) and a quasi-two dimensional (2D) Van der Waals antiferromagnet (AFM). We find that the interaction between a surface Dirac plasmon polariton in the 3D TI and a magnon polariton in the 2D AFM is mediated by the phonon coupling in the 3D TI material and can result in emergence of a new hybridized mode, namely a surface Dirac plasmon-phonon-magnon polariton. We numerically study the dependence of the strong coupling on a variety of structural parameters of the 3D TI / 2D AFM hybrid material. Our results reveal that the strength of the coupling depends primarily on the anisotropy constant of the 2D AFM material, as well as on its thickness, and reaches a maximum when the AFM layer is sufficiently thick to be considered a half-infinite slab. We show that the extremely large anisotropy constant reported for certain 2D van der Waals AFMs results in a coupling strength that should be experimentally observable even in the presence of realistic scattering losses.

I. INTRODUCTION

The tremendous progress in materials science and engineering in recent years has resulted in the synthesis of numerous new classes of materials with unprecedented properties and the potential to develop new devices that address the "THz gap" in optoelectronic device technologies in an important region of the electromagnetic spectrum[1–10]. For instance, three dimensional topological insulators (3D TIs) such as Sb_2Te_3, Bi_2Te_3 or Bi_2Se_3, which host two-dimensional surface Dirac plasmons with energy in the THz regime, could be utilized to guide THz signals within integrated circuits [11–14]. Similarly, two-dimensional van der Waals antiferromagnetic (2D AFM) materials like $FePS_3$, $NiPS_3$, $MnBi_2Te_4$, or CrI_3, which host magnons in the same THz energy range, could be employed to transfer THz frequency information without energy dissipation due to the absence of charge current [15–22]. However, to date the generation of THz magnons in AFM materials is still not well controlled, with common techniques relying on conversion from a thermal source [23–26]. Moreover, the magnon in an AFM material is insensitive to small external magnetic fields because of a vanishing macroscopic magnetic moment. Those material properties make it difficult to utilize magnons in AFMs within devices. Finding ways to generate, control, and detect magnons in an AFM material-based heterostructure is therefore one essential step toward improved devices. In that context, a strong interaction between the electric and magnetic degree of freedoms in a TI/AFM heterostructure, which

results in a hybridization between the magnetic and plasmonic resonances of the two constituents, may provide an effective alternative for the excitation, manipulation, and detection of the magnon via optical control of the dispersion of surface plasmons in the TI. Moreover, the hybridization of magnons with photons [27–30] or phonons [21, 26] could lead to emergent properties that offer even more device opportunities.

We numerically study the emergence of strong coupling between THz excitations in a 3D TI / AFM hybrid material. Specifically, we consider hybridization of two excitations: the Dirac plasmon-phonon polariton (DPPP) on the surface of a 3D TI and a magnon polariton (MP) in an AFM. The DPPP on the surface of 3D TI is itself a hybridized state, as described below, and such polaritons have been studied extensively [31–37]. MPs, which are the collective excitations of electronic spins in a magnetic material (i.e. spin waves), have also been studied extensively in numerous material platforms [38–43]. To date there have been just a few reports on the interaction between the surface DPPP and the MP in heterostructures composed of a 3D TI and an AFM, and these have been limited to 3D antiferromagnetic materials such as NiO, FeF_2, or MnF_2 [44–46]. The computationally-predicted anticrossing splitting in the systems studied to date is too small to be observed experimentally. In other words, these previous reports suggest that it will not be possible to create hybridized states or reach the strong coupling regime in such systems with presently available materials.

We show that three changes to the 3D TI / AFM hybrid material composition and structure allow for entry into the regime in which strong coupling should be experimentally observable. First, we consider 2D van der Waals AFMs such as $FePS_3$, which has an anisotropy energy with magnitude between 2.66 meV and 3.6 meV [26, 47–50], up to three orders of magnitude

larger than that of a typical 3D antiferromagnetic material like MnF$_3$. This remarkably large anisotropy energy significantly increases the strength of coupling between the magnon polariton in the 2D AFM and the surface DPPP in a 3D TI. The relatively high magnon energy ($\approx$ 3.7 THz) in FePS$_3$ [26, 51] also reduces the need for an extremely high quality 3D TI such as that reported previously for a hybrid composed of a 3D TI and a traditional 3D AFM [46]. Second, increasing the thickness of the AFM material allows one to tune the number of magnons in the hybridized states, which in turn increases the coupling constant. Third, the coupling of an electromagnetic wave with a phonon in the bulk of a 3D TI allows one to tune the energy of the DPPP by changing the thickness of the TI. This provides a tool for tuning the DPPP toward resonance with the MP in the AFM material, thereby enhancing the strength and visibility of the coupling between the excitations in the two materials.

The paper is organized as follow. In Sect. II, we present the methods and models employed to investigate the interaction between the 3D TI layer and the 2D AFM material. We first introduce a conceptual model and computational framework for studying the anticrossing between hybridized states of a DPPP and MP. We next introduce the optical response functions of TIs and AFMs to the electric and magnetic components of an electromagnetic wave propagating within each constituent material. We end Sect. II with a description of the global scattering matrix method we employ to solve Maxwell's equations within the TI / AFM heterostructure and compute a dispersion relation describing the dependence of the energy (or frequency) of the excitations ($E(k)$ / $\omega(k)$) on the wave vector k. In Sect. III we discuss the calculated dispersion relations for the surface DPPPs. We explore the dependence of these dispersion relations on various material properties and, in particular, explore the material and device properties required to obtain strong coupling between the 3D TI and the 2D AFM heterostructure. The roles of the material parameters in tuning the strength of this coupling provide important guidance as to how the strong coupling regime can be reached experimentally. Finally, we provide conclusions and perspectives for this work in Sect. IV.

II. THEORY AND MODEL

A. Conceptual Framework

Hybridized states are established when two distinct excitations interact with sufficient strength to create a new mode whose character and dispersion relation cannot be understood by considering either excitation alone [33, 52, 53]. A good example is the formation of a surface plasmon polariton, which is a hybridized state formed from an electromagnetic wave (photon) and charges oscillating at a metallic sample surface (plasmon). The emergence of such a hybridized state is typically observed through an anti-crossing (avoided crossing) in the dispersion relation. The strength of the interaction can be parameterized by the amplitude of the avoided-crossing splitting between the two polariton branches. By analogy to cavity quantum electrodynamics, we define strong coupling to be the regime in which the observed mode splitting δ becomes comparable to the line width of the involved excitation, making the cooperativity factor $C = \frac{\delta^2}{4\Gamma_1\Gamma_2} \geq 1$ [54], where Γ_1 and Γ_2 are the line widths of the isolated excitations that comprise the hybridized states. These line widths originate in the loss (dissipation) for each excitation.

Tuning the DPPP into resonance with the MP results in stronger and more easily observable coupling. This can be understood conceptually from a 2×2 matrix Hamiltonian:

$$\hat{H} = \begin{bmatrix} E_{DPPP}(k, d_{TI}) & V_{int} \\ V_{int} & E_{MP}(k) \end{bmatrix} \qquad (1)$$

where $E_{DPPP}(k, d_{TI})$ is the energy of the DPPP in the TI, which depends on the wave vector k and the TI thickness d_{TI}, E_{MP} is the energy of the magnon polariton in the AFM, and V_{int} is the strength of the coupling between the DPPP and the MP. The energies of the hybridized state that arises due to coupling are found from the eigenvalues of this matrix. The eigenstates are the hybridized modes with both DPPP and MP characterized, i.e the superposition $\Psi_{Hybrid} = \Psi_{TI} + \Psi_{AFM}$ where Ψ_{TI} and Ψ_{AFM} describe the surface Dirac plasmon-phonon-polariton state in the TI and the magnon polariton state in the AFM, respectively.

When E_{DPPP} and E_{MP} are significantly different, the eigenstates remain largely dominated by either the DPPP or MP modes. The perturbation induced by the coupling is small and difficult to distinguish from the normal k-dependence of the energy for the independent DPPP or MP. In other words, the two excitations are only weakly coupled. Two factors impact the strength and visibility of the coupling. First, when d_{TI} is chosen so that $E_{DPPP}(k)$ and $E_{MP}(k)$ are degenerate for some value of k, the eigenstates at the degeneracy point have energy $E_{DPPP}(k) \pm V_{int}$ (which is equal to $E_{MP}(k) \pm V_{int}$ for this value of k). In other words, the eigenstates are fully hybridized polaritons with equal DPPP and MP composition. For this reason, the dependence of the DPPP energy on d_{TI} provides a powerful tool for tuning the excitations into resonance and creating a fully hybridized state. Second, the magnitude of the interaction parameter V_{int} controls the magnitude of the anti-crossing splitting ($\delta = 2V_{int}$). As we will show below, the choice of a 2d AFM with large anisotropy energy and an increasing thickness of the AFM material both increase the strength of the interaction between magnons and the EM wave.

B. Computational Framework

An EM wave will excite both surface Dirac plasmon phonon polaritons (DPPPs) in the TI and magnon polaritons (MPs) in the AFM via its electric and magnetic field components. Those excitations will interact with each other, resulting in the hybridization between plasmon-phononic and magnetic resonance, namely the creation of surface Dirac plasmon-phonon-magnon polaritons (SDPP-MPs) that lead to changes in the dispersion relationship $\omega(k)$. We compute these dispersion relations using a global scattering matrix that allows us to a) find a solution to Maxwell's equations for an electromagnetic (EM) wave propagating in the considered structure subject to standard boundary conditions at interfaces and b) pull out information about the electric field amplitudes at any point or interface within the heterostructure. From the output of this technique we plot the imaginary part of the reflection coefficient, which describes the amplitudes of the evanescent waves propagating along the surface of the TI layer as a function of inplane wave vector and the frequency of EM wave. Local maxima of the imaginary part of the reflection coefficient represent the existence of the modes and thus this type of plot effectively reveals the dispersion relation. Analysis of the dispersion relationships for these hybridized modes as a function of the structural parameters allows us to explore the physical origins of the interactions. The inputs for this global scattering method are the optical response function and thickness of the corresponding material constituents of the system, which we present next.

C. Optical response function: TI

We consider two potential 3D TI materials, Bi_2Se_3 and Sb_2Te_3, that host two dimensional spin-polarized Dirac plasmon on the surface. The behavior of these Dirac plasmon is analogous to that in graphene and the Dirac plasmon system on the surface of a pristine 3D TI layer can be treated as a conducting electron sheet with optical conductivity given by

$$\sigma_{\text{TI}} = \frac{e^2 E_F}{4\pi\hbar^2} \frac{i}{\omega + i\tau^{-1}}. \tag{2}$$

where $E_F \approx 260\ meV$ is the Fermi energy of surface states, $\tau \approx 0.06\ ps$ is the relaxation time [37], and e is the electron charge.

We note that a TI thin film can acquire a nonzero local magnetic moment due to proximity with an AFM material when the two materials are put in contact. However, this effect is normally weak and can be neglected, especially in the case of an AFM material [55]. In addition, the hybridized states at the interface between a TI and another material (e.g. the AFM in this work) may change the carrier density at the interface, as predicted by density functional theory for the case of a TI/III-V semiconductor interface[56]. In the case of a structure composed of two van der Waals materials, this effect is expected to be small and can be ignored. We therefore assume the same optical conductivity expression for the conducting surface of the TI and the interface between the TI and the AFM. In other words, in the following $\sigma_0 \equiv \sigma_1 \equiv \sigma$ as given by Eq. 2 (where σ_0 and σ_1 are respective the optical conductivity of the Dirac plasmon on the surface of the TI and at the interface between the TI and the AFM).

Remarkably, interactions between the Dirac plasmon mode and the lattice vibrations, i.e. phonons, in a bulk TI significantly alter the dispersion of the surface Dirac plasmon polariton in the TI, resulting in the formation of a Dirac plasmon phonon polariton (DPPP) mode that is different from the polariton modes of 2D materials like Graphene [12, 34]. In the case of chalcogenide materials with a rhombohedral lattice and quantum layer structure, like that of Bi_2Se_3 and Sb_2Te_3, two characteristic phonon modes are observable when the AC electric field is perpendicular to the c axis: the alpha phonon, also known as the (Eu1) mode, and the beta phonon, also known as the (Eu2) mode [57]. The strong alpha phonon mode oscillation contributes to a large variation in the TI permittivity in the THz regime we consider in this work. In contrast, the contribution of the beta phonon is usually small and is negligible for the case of Sb_2Te_3. Incorporating all of these effects, the frequency-dependent permittivity of the bulk TI in the far-IR range of interest can be described by the Drude–Lorentz model [37, 46, 56]:

$$\varepsilon_{TI} = \varepsilon_\infty + \frac{S_\alpha^2}{\omega_\alpha^2 - \omega^2 - i\omega\Gamma_\alpha} + \frac{S_\beta^2}{\omega_\beta^2 - \omega^2 - i\omega\Gamma_\beta} \tag{3}$$

where ε_∞ is the dielectric constant at high frequency ($\omega \to \infty$), ω_x, Γ_x, and S_x are the frequency, the scattering rate, and the strength of the Lorentz oscillator associated with the α ($x = \alpha$) and the β ($x = \beta$) phonons of the TI thin film. Numerical values for all TI parameters are taken from reference [36] and are listed in Table I. All the TIs used in this work are non-magnetic materials, so their permeabilities are set to unity, $\mu_{TI} = 1$.

D. Optical response function: 2D AFM

The AFM materials we consider ($FePS_3$, $MnPS_3$, $NiPS_3$, and $CoPS_3$) belong to a family of quasi-two-dimensional van der Waals AFMs in which the magnetic lattice is a honeycomb-like structure akin to graphene [19, 20]. One of the important theoretical advances reported here is that we use a Heisenberg Hamiltonian

TABLE I. The TI parameters used in this work, taken from [36].

Materials	ε_∞	$S_\alpha(\mathrm{cm}^{-1})$	$\omega_\alpha(\mathrm{cm}^{-1})$	$\Gamma_\alpha(\mathrm{cm}^{-1})$	$S_\beta~(\mathrm{cm}^{-1})$	$\omega_\beta(\mathrm{cm}^{-1})$	$\Gamma_\beta~(\mathrm{cm}^{-1})$
Bi_2Se_3	1	675.9	63.03	17.5	100	126.94	10
Sb_2Te_3	51	1498.0	67.3	10	NA	NA	NA

model that captures the magnetic interactions in the quasi 2D AFM material to derive an analytical expression for the magnetic susceptibility tensor of $FePS_3$. This analytical expression is generalizable to any 2D AFM material in the family XPS_3 (X=Mn, Fe, Co, Ni). This magnetic susceptibility tensor, which is the input for our global scattering matrix method, is distinct from that of bulk (3D) AFM materials because one has to consider interactions between the spin moments of magnetic atoms up to the third next-nearest-neighbor. See Appendix A for details.

Because van de Waals layered structures have very weak interlayer coupling, the dielectric tensor of $FePS_3$ is frequency independent in the AFM phase and has a strong anisotropy between the in-plane and out-of-plane dielectric constants of the bulk materials, which can be written as

$$\varepsilon_{AFM} = \begin{pmatrix} \varepsilon^{xx} & 0 & 0 \\ 0 & \varepsilon^{yy} & 0 \\ 0 & 0 & \varepsilon^{zz} \end{pmatrix} \qquad (4)$$

where $\varepsilon^{xx} = \varepsilon^{yy} = \varepsilon^{\parallel} = 25$ and $\varepsilon^{zz} = \varepsilon^{\perp} = 5$ [58]. Below the Neel temperature of $T_N = 123~K$ [59], the magnetic moment of $FePS_3$ is out of plane along the c-direction (z-direction). We assume that the samples are below their Neel temperatures in the calculations we conduct here. The permeability of $FePS_3$ in the absence of an external magnetic field therefore can be expressed as

$$\mu = \begin{bmatrix} \mu^{xx} & 0 & 0 \\ 0 & \mu^{yy} & 0 \\ 0 & 0 & 1 \end{bmatrix} \qquad (5)$$

where $\mu^{xx} = \mu^{yy} = 1 + 4\pi \frac{2\gamma^2 H_a M_0}{\Omega_0^2 - (\omega + i/\tau_{mag})^2}$, and $\mu^{zz} = 1$. See Appendix A for the detailed derivation of Eqn. 5. Here, γ is the gyromagnetic ratio, H_a is the effective anisotropy field, M_0 is the sublattice magnetization saturation, Ω_0 is the antiferromagnetic resonance or zero-wave vector magnon frequency in the AFM material, and τ_{mag} is the magnetic relaxation time. For $FePS_3$, $M_0 \approx 830~G$, $H_a = 9840~kOe$, $\Omega_0 = 3.7~THz$, and $\Gamma_{AFM} = 1/\tau_{mag} = 0.035~THz$ [21]. Below we will consider how the scattering loss rate in the AFM material influences the strength of the coupling between the TI and AFM materials. Finally, the substrate MgO used in this study is a non-magnetic material so that its permeability $\mu_{MgO} = 1$ and its dielectric constant is given by $\varepsilon_{MgO} = 9.9$ [60].

E. Global scattering matrix approach

Now that we have obtained the optical response functions for the material constituents of our hybrid structure, we study the interaction between the TI and the AFM constituents by solving Maxwell's equations to derive the dispersion relationship for a monochromatic electromagnetic (EM) wave propagating in our optical structure. We do this using the scattering matrix formalism that has proven to be a powerful tool for investigating the electric and spin transport properties of layered structures [61–63]. Here we adapt that robust tool to our optical structure. We note that we have previously used a recursive method [46, 56] to efficiently calculate the transmission and reflection coefficients of hybrid structures, but this recursive approach does not make it easy to pull out what happens at specific interfaces within the structure. The ability to isolate and understand what happens at interfaces within the structure, or in subsets of the structure, provides important insight into the underlying physics and the ways in which the structure and composition can be used to tune the optical response. We therefore develop here a new so-called "global scattering matrix" method from which we can easily extract what happens at each interface and within each layer. We present a detailed description of the global scattering matrix formalism in Appendix B. The most important outcome of this formalism for the work presented here is that we can compute the optical response of the entire structure and the constituent parts from a global scattering matrix constructed based on interfacial scattering and propagation matrices that capture what happens at each interface and within each layer of the structure. The inputs to these interfacial scattering and propagation matrices are the materials parameters of the system and the optical response functions of each layer.

Starting from the optical response functions derived in the previous sections, we employ the global scattering matrix formalism to compute the reflection coefficients for our hybrid material system. The imaginary part of the reflection coefficient, $Im(r)$, is proportional to the losses in the system [37, 56, 64–67]. The presence of loss in the reflectance spectrum indicates that the incident EM wave has generated an excitation that is carrying energy away laterally, i. e., propagating in the x- or y-direction rather than transmitting or reflecting in the +z or -z directions, respectively. The frequency dependence of such loss thus generates the dispersion curves for the hybridized excitations in the coupled system, which is the aim of this study. In the next section we consider how this dispersion relation depends on structural and

material properties, which allows us to probe the physics underlying the formation of hybridized excitations.

III. RESULT AND DISCUSSION

The structure under investigation in this paper is shown in Fig. 1: an AFM material (FePS$_3$) on a substrate (MgO) is capped with a TI thin film. In this model, an electromagnetic wave with both TE- and TM-polarized components is incident on the top TI layer. As a result of the electromagnetic interaction with the electric and magnetic field components of the EM wave, surface Dirac plasmon polaritons in the TI thin film and magnon polaritons in the AFM material will be excited at certain resonant frequencies. The excited surface Dirac plasmon polaritons can then interact with the phonon in the bulk of the TI and also couple to the magnon polaritons in the AFM layer. We note that the TE-polarized EM wave cannot excite the surface Dirac plasmon polaritons in the TI [56]. Consequently we consider only TM-polarized incident EM waves in the our analysis. For convenience, we denote the Cartesian coordinates as in Fig. 1: the z-axis is along the growth direction of the structure, the heterostructure has finite width W in the x direction, and the heterostructure is infinite in the y-direction. We set the direction of propagation of the EM wave to be parallel to the x-z plane so that the magnetic field of TM-polarized EM waves is along the y axis. Throughout our analysis the color plots in the following figures represent the amplitude of the imaginary part of the Fresnel reflection coefficient $Im(r)$ of the entire structure. The maxima of the function $Im(r)$ reveals the dispersion relationship for the coupled modes. We first discuss the emergence and characteristics of coupled surface Dirac plasmon-phonon-magnon modes and then consider how the strength of the coupling depends on structural and material parameters.

We first note that in the long-wavelength limit ($k_x d_{TI} \ll 1$), the analytical expression for the surface Dirac plasmon mode in the TI thin film was derived in [12, 13]

$$\omega_{TI_+}^2 = \frac{v_F \sqrt{2\pi n_{2D}} e^2}{\varepsilon_0 h} \frac{k_x}{\varepsilon_{top} + \varepsilon_{bot} + k_x d_{TI} \varepsilon_{TI}} \quad (6)$$

and

$$\omega_{TI_-}^2 = \frac{2\varepsilon_0 \varepsilon_{TI} h v_F + e^2 \sqrt{2\pi n_D} d_{TI}}{\sqrt{4\varepsilon_0^2 \varepsilon_{TI}^2 h^2 v_F^2 + 2\varepsilon_0 \varepsilon_{TI} e^2 \sqrt{2\pi n_D} d_{TI}}} k_x^2 \quad (7)$$

where the subscripts TI_+ and TI_- stand for the optical and acoustic mode, respectively. Here v_F is the Fermi velocity for the Dirac plasmon in the TI; n_{2D} is the sheet carrier concentration of the entire TI thin film, including the contribution from both surfaces; ε_{top}, ε_{bot} and ε_{TI} are the permittivity of the top and bottom dielectric media and the TI, respectively; k_x is the in-plane wave vector;
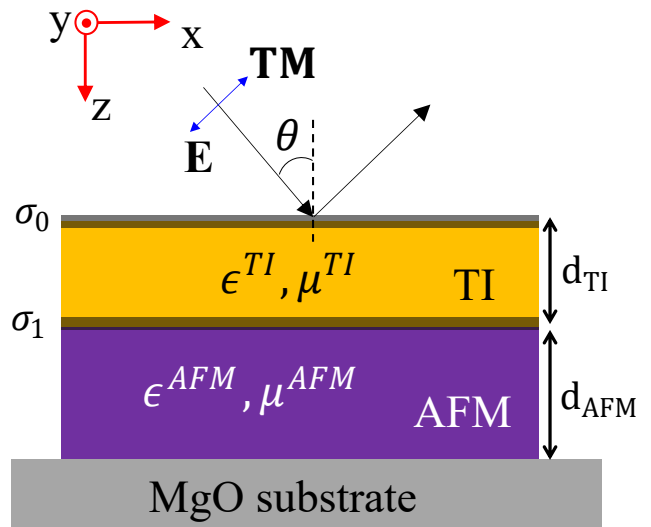

FIG. 1. The TI/AFM bilayer structure on an MgO substrate investigated here. The optical response functions in each material are the permittivity $\varepsilon_{TI/AFM}$ and permeability $\mu_{TI/AFM}$. An EM wave with both TE- and TM-polarization is incident on the TI from above with angle of incidence θ. However only TM-polarized light will excite both electric and magnetic degrees of freedoms in the structure, namely surface Dirac-plasmon-phonon polaritons in the TI and magnon polaritions in the AFM.

and d_{TI} is the thickness of the TI layer. In this work, we focus on studying the optical mode of the surface Dirac plasmon in the TI; only this mode can be excited in a traditional optical experiment because the acoustic mode does not have any contribution in the optical dipole matrix element [13]. In the following parts we will use relation 6 as a reference for our further analysis of the hybridized modes.

A. Surface Dirac plasmon-phonon-magnon polariton: Signature of strong coupling

We will start by treating the AFM as a semi-infinite slab (i.e. infinitely thick) so that we can focus on the physics of the TI/AFM interface and the effect of the TI parameters on the resulting emergent hybridized state. We apply the global scattering matrix technique described in Sect. II E to two different configurations of the structure shown in Fig. 1: 1) a Sb$_2$Te$_3$ layer with thickness $d_{TI} = 500$ nm on a half-infinite bare MgO substrate and 2) the same Sb$_2$Te$_3$ layer with thickness $d_{TI} = 500$ nm on a half-infinite FePS$_3$ material [the thickness of the FePS$_3$ is very large in comparison to that of the Sb$_2$Te$_3$ layer so that, in these calculations, $d_{AFM} \approx 10 d_{TI}$)]. The color plot in Fig. 2 displays the imaginary part of the Fresnel reflection coefficient $Im(r)$ calculated for the entire structure as a function of the the frequency ω and the in-plane wave vector k_x.

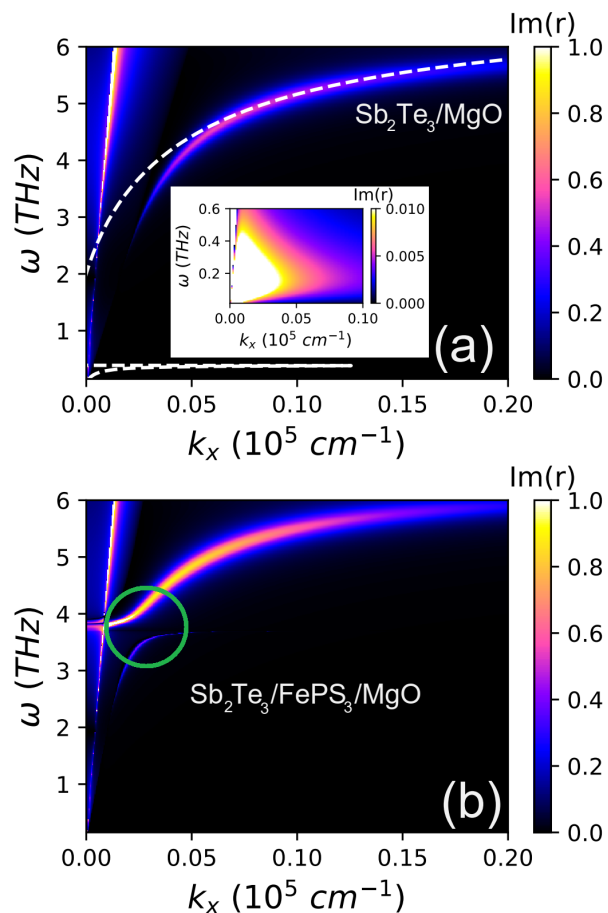In Fig. 2(a) we plot the dispersion relation for the sur-

FIG. 2. (a) The dispersion relation of the surface Dirac plasmon-phonon polariton in a bare Sb_2Te_3 thin film on the half-infinite MgO substrate. The dashed white line provides, for reference, an analytical calculation of the dispersion of the surface Dirac plasmon mode in a pristine Sb_2Te_3 layer on a MgO substrate, as described in the text. The inset shows the existence of the mode at 0.2 THz, which is $\sim$100x weaker than the modes at higher frequency. (b) The surface Dirac plasmon-phonon-magnon polariton in the $Sb_2Te_3/FePS_3$ structure. Both dispersion relations are plotted as a function of in-plane wave vector k_x and frequency ω. These calculations were both performed with the thickness of the TI thin film $d_{TI} = 500\ nm$ and the $FePS_3$ layer in figure (b) is sufficiently thick to be considered a semi-infinite layer.

face Dirac plasmon-phonon polariton (SDPPP) in a bare Sb_2Te_3 layer on the half-infinite MgO substrate. The dispersion of the SDPPP appears in the color plot in the range between $k_x = 0.02 \times 10^5\ cm^{-1}$ and $0.2 \times 10^5\ cm^{-1}$. The steeper line in the color plot between $k_x = 0$ and $0.02 \times 10^5\ cm^{-1}$, in both this and subsequent figures, is the dispersion of the photon in vacuum $\omega = ck$. This photon dispersion is not important to the focus of this work and we normally neglect it without further notification. The dashed white curve is an analytical calculation of the dispersion of the surface Dirac plasmon mode in a pristine Sb_2Te_3 layer on a half-infinite MgO sub-

strate obtained by using Eq. 6. One can see that the dispersion of the SDPPP represented in the color plot in Fig. 2(a) is comparable to the analytical curve, with very good agreement for polariton branches above 2 THz. We note that beside the upper surface Dirac plasmon-phonon polariton branch with frequency above 2 THz, which can be observed clearly in the Fig. 2(a) color plot, there is also a mode at around 0.2 THz shown in the inset. This lower polariton mode can be seen clearly from the dashed white analytical curve around 0.2 THz (the horizontal dashed white line) in the Fig. 2(a), but its intensity is two orders of magnitude less than the intensity of the modes above 2 THz. This lower intensity is due to a large scattering loss rate of the surface Dirac plasmon in the Sb_2Te_3 material at room temperature. The surface Dirac plasmon, with high loss, dominates the modes at low frequency and consequently this lower frequency mode is barely visible in our color plot. In contrast, for the higher frequency mode (above 2 THz), the interaction with the α phonon plays an important role and makes the surface Dirac plasmon-phonon polariton mode become visible. Overall, Fig. 2(a) simply verifies that the global scatting matrix approach (color plot) agrees with the analytical dispersion (dashed white line) when applied to a sample in which interactions with the AFM material are suppressed. We will next turn on interactions with the AFM. Because the energy of magnons in the AFMs considered here is far higher than the low-energy Dirac plasmon polariton mode, the interaction between the magnon polariton in the AFM and the TI mode below 2 THz is small and can be ignored.
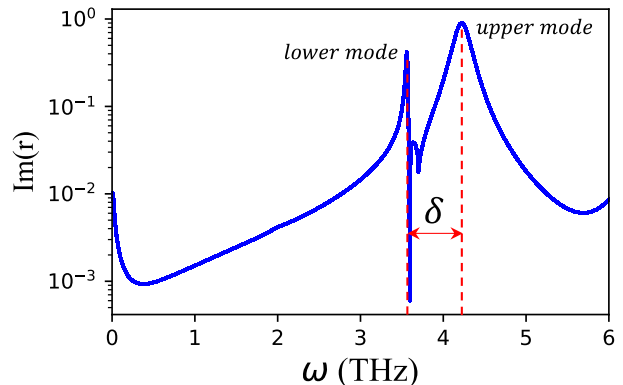

FIG. 3. The imaginary part of the reflectivity Im(r) on a logarithmic (log.) scale as a function of frequency ω calculated for a $Sb_2Te_3/FePS_3$ structure with the thickness of TI thin film $d_{TI} = 500\ nm$ and the $FePS_3$ layer sufficiently thick to be considered a semi-infinite layer. The result is calculated for an plane wave vector $k_x = 0.03 \times 10^5\ cm^{-1}$ around the resonance point for the surface Dirac plasmon-phonon-magnon polariton.

In Fig. 2(b) the Sb_2Te_3 is put on top of a very thick $FePS_3$ layer. We observe a significant change in the spectrum of the dispersion relation around $\omega \approx 3.7\ THz$ owing to the interaction between the surface Dirac plasmon-

phonon polariton (SDPPP) in the Sb_2Te_3 layer and the magnon polariton (MP) in the $FePS_3$. The coupling between the SDPPP and MP results in an anti-crossing highlighted by the green circle in Fig. 2(b). This interaction and anti-crossing lead to the formation of an upper and a lower mode that are evident through the reduction of the amplitude of $Im(r)$ around $\omega = 3.7\ THz$ and $k_x \approx 0.3 \times 10^5\ cm^{-1}$ in the color plot. The magnitude of the splitting between the two modes that occurs at $3.7\ THz$ due to the coupling between the SDPPP and MP can be evaluated by plotting the function $Im(r)$ vs. frequency ω at a fixed $k_x \approx 0.3 \times 10^5\ cm^{-1}$ (resonance point) as shown in Fig. 3. In this plot, the peaks at around $\omega \approx 3.5\ THz$ and $\omega \approx 4.2\ THz$ indicate, respectively, the lower and upper modes in the color plot of Fig. 2(b). The separation between the two peaks denoted by δ is the splitting between the two modes at the resonance point, which is twice the strength of the coupling between the two excitations in our system. The splitting $\delta \approx 0.65\ THz$ extracted from Fig. 3 for the interaction between SDPPP and MP should be experimentally detectable because it is comparable to the line width of the isolated mode in the system. This interaction is entering the strong coupling regime if the cooperativity factor $C = \frac{\delta^2}{4\Gamma_{TI}\Gamma_{AFM}}$ is greater than 1, where Γ_{TI} and Γ_{AFM} are, respectively, the scattering loss rates of the Dirac Plasmon phonon polariton in the TI and the magnon polariton in the AFM. The full width half maximum line width that represents the scattering loss rate for the surface Dirac plasmon phonon polariton in the TI is $\Gamma_{TI} \approx 3\ THz$ [56]. The line width of the magnon polariton in the $FePS_3$ is $\Gamma_{AFM} = 0.035\ THz$ [21]. Inputting these values results in a cooperativity factor $C \approx 1$, which indicates the formation of a hybridized state that is approaching the strong coupling regime.

B. Dependence of the coupling strength on the TI thickness: the role of the phonon in the TI

Our primary aim in this study is to explore the material and structural parameters that enable us to reach the strong coupling regime for the interaction between THz excitations in a TI/AFM structure. We will now investigate the impact of TI structural parameters on the strength of the coupling between the surface Dirac plasmon phonon polaritons (SDPPPs) and magnon polaritons (MPs) in our system. In this section we maintain the very large thickness of the AFM, i.e. the AFM is always a half-infinite medium while the TI's thickness is varied to understand how d_{TI} influences the strength of the coupling. In Fig. 4 we plot the dispersion relation of hybridized surface Dirac plasmon phonon magnon polaritons (SDPP-MPs) for different thicknesses of the TI layer (a) $d_{TI} = 500\ nm$, (b) $d_{TI} = 200\ nm$, and (c) $d_{TI} = 0.5\ nm$. We note that $d_{TI} = 0.5\ nm$ is about the thickness of a single quintuple layer of Sb_2Te_3, which is the minimum practical thickness. One observes from
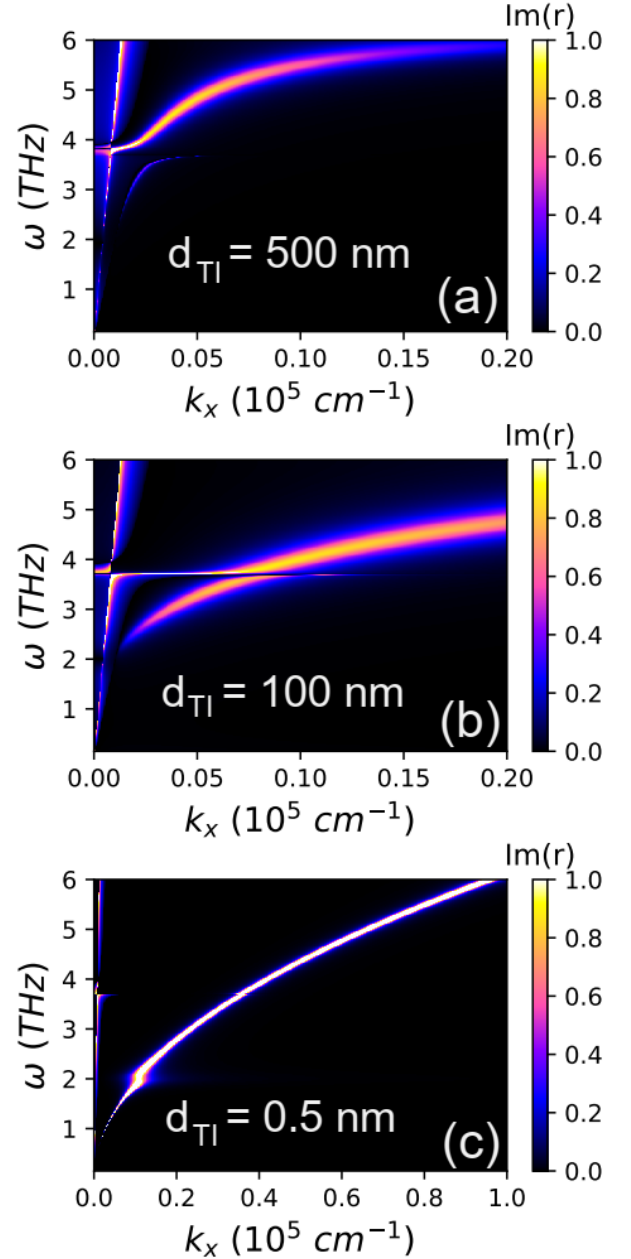

FIG. 4. The imaginary part of the reflectivity $Im(r)$ as a function of frequency ω calculated for a $Sb_2Te_3/FePS_3$ structure with TI thickness (a) $d_{TI} = 500\ nm$, (b) $d_{TI} = 100\ nm$, and (c) and $d_{TI} = 0.5\ nm$ on top of a semi-infinite $FePS_3$ layer.

those plots that the dispersion of SDPP-MPs redshifts, i.e. shifts toward the low frequency regime, as the thickness of the Sb_2Te_3 layer is reduced. This arises as a result of the interaction between the α phonon and the surface Dirac plasmon polaritons in the TI thin film, which makes the dispersion of the surface Dirac plasmon polaritons become thickness-dependent. Indeed, due to a strong coupling between the EM wave and the α phonon in the TI, the real part of the dielectric constant of the TI at low frequency possesses a transition from positive to

negative sign when the frequency ω of EM wave increases from zero and crosses 2 THz for both Bi_2Se_3 and Sb_2Te_3 TI materials, as shown in Fig. 5. When the ω keeps increasing, the dielectric constant becomes positive again and converges to the ε_∞. For the Sb_2Te_3 considered here, the dielectric constant is negative in the range between $2\ THz$ and $6\ THz$, which is why the SDPP-MP mode above 2 THz redshifts as the TI thickness decreases. This dependence can also be seen in the analytical expression for the surface Dirac plasmon mode in Eq. 6 where the thickness of the TI and its dielectric constant appear simultaneously in the denominator. Physically, this redshift occurs because the surface Dirac plasmon polariton modes in the TI are coupled modes of the two surfaces. The energy of that coupled modes depends on the coupling constant, which is proportional to both the dielectric constant and the thickness of the TI.
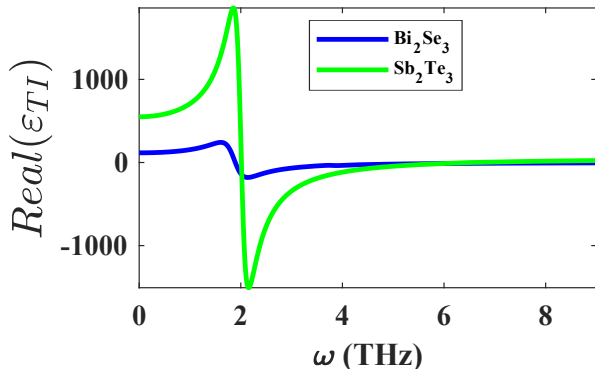

FIG. 5. Dielectric function (real part) of Bi_2Se_3 (blue) and Sb_2Te_3 (green) as a function of frequency plotted using Eq. 3.

A direct consequence of the dependence of the SDPP-MPs on the thickness of the TI thin film is that the strength of the coupling between the surface Dirac plasmon phonon polariton (SDPPP) and the magnon polariton (MP), which is measured by the magnitude of the splitting between the upper and lower mode at $3.7\ THz$, reduces as the thickness of TI decreases. This reduction occurs because the SDPPP shifts away from the resonance with the MP, thus reducing the contribution of the magnon to the hybridized mode and reducing the coupling strength [46]. We note that Fig. 4(c) effectively describes the dispersion relation of a surface Dirac-plasmon-magnon-polariton in a Graphene-like/AFM system. This is because the thickness of the TI is vanishingly-small in this case, creating a degeneracy of the two surfaces of the TI and creating a Graphene-like system with extremely small coupling strength compared to that of the Sb_2Te_3 materials with finite thickness (e.g. $d_{TI} = 500\ nm$). The analysis here reveals the important role of the phonon in the TI as a mediator of the interaction between the surface Dirac Plasmon-phonon polariton in the TI and the magnon polariton in the AFM.
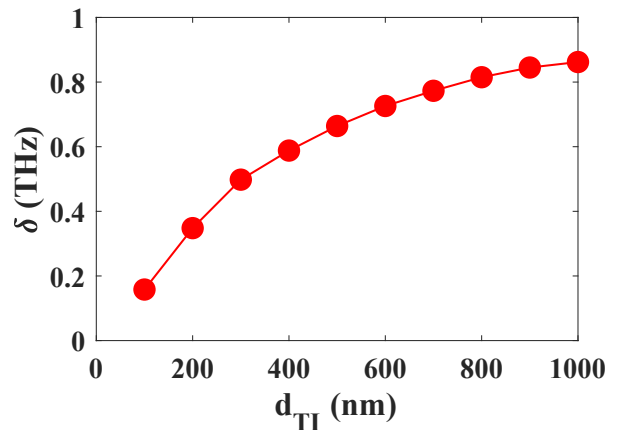
Using the TI's thickness to tune the coupling strength

FIG. 6. Splitting δ indicating the strength of the coupling between the surface Dirac plasmon phonon polariton in the Sb_2Te_3 and the magnon polariton the the $FePS_3$ as a function of the Sb_2Te_3 thickness. This calculation is done with the assumption that the $FePS_3$ layer is very thick and can be considered as a half-infinite medium.

between the surface Dirac Plasmon-phonon polariton in the TI and the magnon polariton in the AFM provides a significant advantage relative to what could be achieved using graphene instead of a TI. Specifically, one can enhance the interaction and reach the strong coupling regime by varying the TI's thickness whereas the coupling strength for a graphene/AFM structure is fixed. Our analysis also indicates that pursuing a TI with larger negative dielectric constant in the frequency regime in which the hybridized mode is formed would reduce the time required to grow the TI sample: a larger coupling strength could be achieved with a thinner TI material. Specifically Sb_2Te_3 is a much better candidate than Bi_2Se_3 for this application because the stronger interaction with the α phonon in Sb_2Te_3 leads to larger magnitude of the real part of the permittivity, as can be seen in Fig.5. Finally, to get a more complete picture of the TI thickness-dependent coupling strength we plot in Fig.6 the splitting δ vs the Sb_2Te_3 thickness d_{TI}. The splitting δ simply rises monotonically without saturation upon increasing d_{TI} across this range of sample thicknesses, from $\delta \approx 0.18\ THz$ at $d_{TI} = 100\ nm$ up to $\delta \approx 0.9\ THz$ when $d_{TI} = 1000\ nm$. This calculation shows that $d_{TI} \geq 400\ nm$ would give a splitting $\geq 0.6\ THz$ that should be experimentally observable and get us into the strong coupling regime for the interaction between THz excitations in the $Sb_2Te_3/FePS_3$ structure.

C. Dependence of the coupling strength on 2D AFM structure parameters and material quality

We now consider the influence of the AFM material properties and structural parameters on the interaction between the surface Dirac plasmon phonon polariton (SDPPP) and the magnon polariton (MP) in the
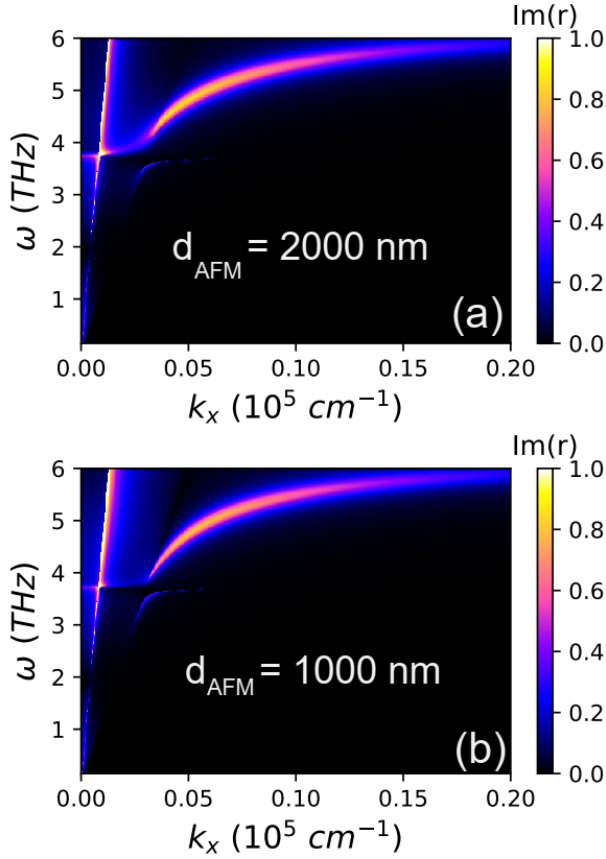
FIG. 7. The imaginary part of reflectivity Im(r) as a function of frequency ω calculated for $Sb_2Te_3/FePS_3$ structure with the thickness of TI thin film $d_{TI} = 500$ nm and the thickness of the $FePS_3$ layer (a) $d_{AFM} = 2000$ nm and (b) $d_{AFM} = 1000$ nm.
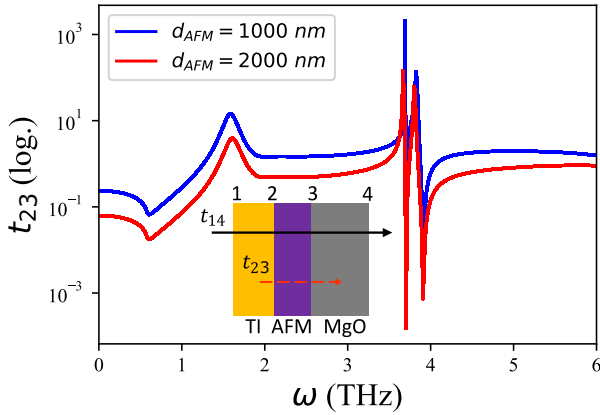

FIG. 8. Transmission coefficient t_{23} as a function of frequency ω at fixed wave vector $k_x = 0.03 \times 10^5$ cm^{-1} for $d_{AFM} = 500$ nm (blue) and $d_{AFM} = 200$ nm (red). The inset represents the TI/AFM structure and indicates how the transmission coefficient is calculated for different paths.

TI/AFM structure. To do this, we replace the semi-infinite AFM slab with a slab of finite thickness on a

semi-infinite MgO substate. The dispersion relations shown in Fig.7 are calculated by applying the global scattering matrix method with a fixed Sb_2Te_3 thickness of $d_{TI} = 500$ nm for different thickness of the $FePS_3$ layer (a) $d_{AFM} = 2000$ nm and (b) $d_{AFM} = 1000$ nm.
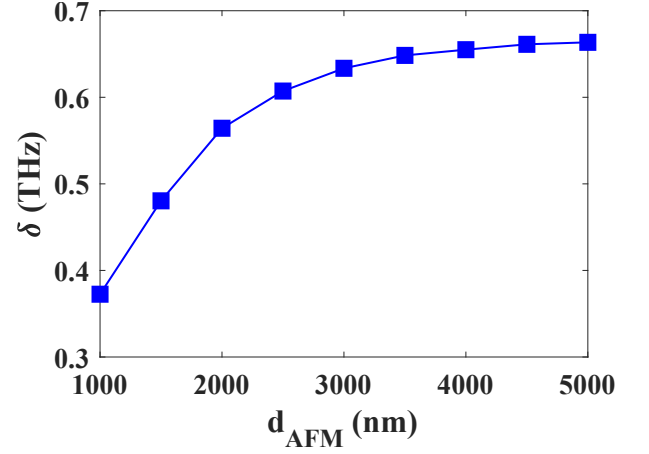

FIG. 9. Splitting δ indicating the strength of the coupling between the surface Dirac plasmon phonon polariton in the Sb_2Te_3 and the magnon polariton in the $FePS_3$ as a function of the $FePS_3$ thickness. This calculation is done for fixed Sb_2Te_3 thickness $d_{TI} = 500$ nm.

We previously saw that decreasing the thickness of the TI redshifted the SDPPP mode, which in turn altered the strength of the surface Dirac plasmon phonon magnon polaritons (SDPP-MP) coupling. Varying the AFM thickness does not modify the dispersion of SDPP-MP in the same way. There is no shift in either the MP or SDPPP mode with AFM thickness. However, the coupling strength, as measured by the splitting, increases with increasing AFM thickness. To understand what is happening in this case, we plot in Fig. 8 the transmission coefficient t_{23}, on a logarithmic scale, for the EM wave travelling between the 2nd and 3rd interfaces. These interfaces are, respectively, (2nd) the interface between the TI and the AFM and (3rd) the interface between the AFM and the MgO substrate, as indicated in the inset of Fig.8. Please refer to Appendix B for a detailed description of how we calculated this transmission coefficient from the global scattering matrix technique. Fig.8 shows the result for $d_{AFM} = 1000$ nm (blue curve) and $d_{AFM} = 2000$ nm (red curve) while keeping $d_{TI} = 500$ nm fixed. One can see that the transmission coefficient t_{23} decreases over the entire range of frequencies upon increasing the thickness of the AFM layer from 1000 nm to 2000 nm. This shows that the thinner $FePS_3$ layer is more transparent to the EM wave. One can think of this in analogy to an optical absorption: there is a fixed interaction probability (cross-section) and consequently the probability of interaction between the EM wave and the magnetic degree of freedom in the AFM layer (MP) increases with AFM thickness. Essentially, a thinner $FePS_3$ results in smaller amplitude of the magnon

polariton mode and thus a smaller interaction between the surface Dirac plasmon phonon polariton in the TI and the magnon polarition in the AFM layer because fewer magnons participate.

We plot the splitting δ as a function of AFM thickness in Fig. 9. One observes that the splitting δ increases rapidly from 0.38 THz at $d_{AFM} = 1000$ nm to 0.6 THz at $d_{AFM} = 2500$ nm. The splitting begins to saturate at $d_{AFM} = 3000$ nm with $\delta \approx 0.64$ THz. The saturation of the splitting occurs because of a competition between two effects. The number of magnons generated continues to increase with increasing AFM thickness. However, the surface electromagnetic wave associated with the SDPPP decays exponentially with z, which means that the cross-section for interaction between the EM wave and the local spin moment also decreases exponentially with z. In other words, magnons generated sufficiently far from the TI/AFM interface do not contribute to the formation of hybridized states and the splitting saturates at $\delta \approx 0.64$ THz when $d_{AFM} = 3000$ nm. Fig. 9 tells us that the FePS$_3$ layer should be thicker than 3000 nm in order to obtain a coupling strength close to the saturation, but that increasing the AFM thickness above this value is unlikely to be useful.

We next consider the impact of the anisotropy constant of the AFM material constituent of the TI/AFM heterostructure. The anisotropy constant is defined by $K = \gamma^2 H_a M_0$, where γ, H_a, and M_0 are, respectively, the gyromagnetic ratio, effective anisotropy field, and magnetization of the AFM spin sublattice. In Fig. 10 we plot the dispersion of the SDPP-MP for $d_{TI} = 500$ nm and $d_{AFM} = 5000$ nm for different values of the anisotropy constant of the AFM material: (a) $K = \frac{1}{10}K_0$, (b) $K = \frac{1}{5}K_0$, and (c) $K = K_0$, where K_0 is the value of anisotropy constant for FePS$_3$ used in our previous calculations. We find that the strength of the TI/AFM coupling is proportional to the magnitude of this parameter K. In other words, a larger value of the anisotropy constant results in stronger coupling and a larger δ, meaning a larger and more easily detectable splitting between the SDPP-MP hybrid modes.

We now explain the physical origin of the increased coupling strength with increasing K shown in Fig 10. The magnitude of the anisotropy constant K determines the magnetic dipole of the AFM material. A larger magnetic dipole leads to a stronger interaction between the magnetic component of the EM wave propagating in the system and the local spin moment in the AFM. A stronger interaction between the magnetic component of the EM wave and the local spin moment means that the EM wave excites magnon polaritons containing a larger number of magnons. The increased number of magnon polaritons results in a stronger interaction between the magnon states in the AFM and the Dirac plasmon phonon states in the TI, resulting in a larger contribution of magnons to the formation of Dirac plasmon phonon magnon hybrid modes. Because the anisotropy constant is primarily determined by the anisotropy energy and spin sublat-
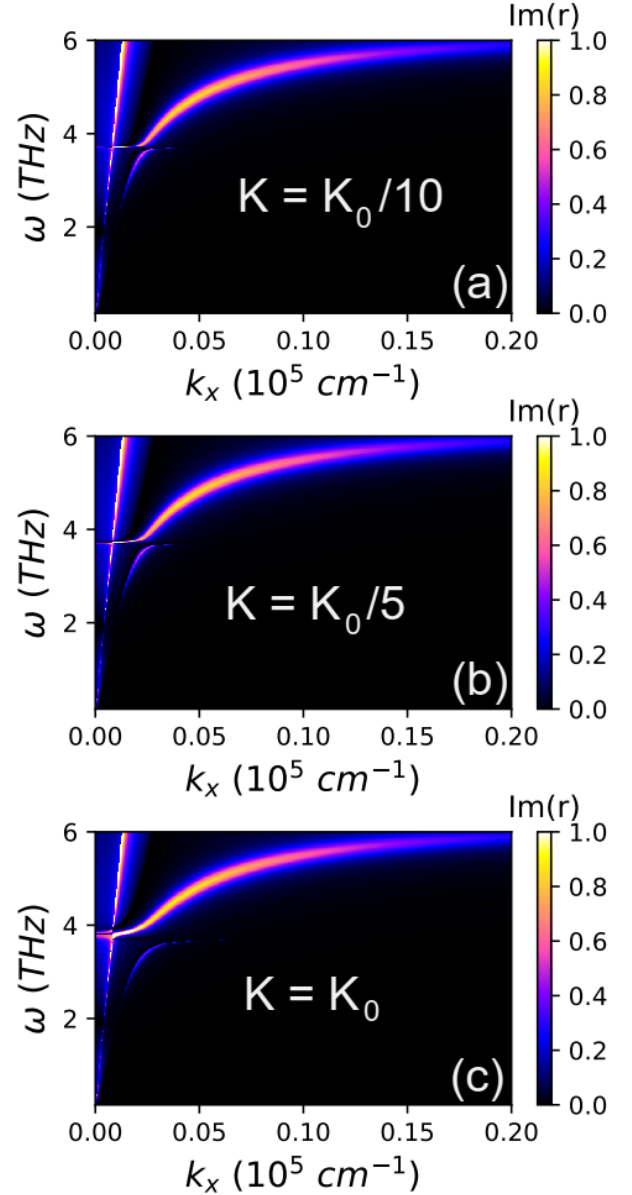

FIG. 10. Dispersion relation of surface Dirac plasmon phonon magnon polariton (SDPP-MP) in Sb$_2$Te$_3$/FePS$_3$ bilayer structure with thickness of Sb$_2$Te$_3$ $d_{TI} = 500$ nm and half-infinite FePS$_3$ layer for different value of anisotropy constant $K = \gamma^2 H_a M_0$ (a) $K = \frac{1}{10}K_0$, (b) $K = \frac{1}{5}K_0$ and (c) $K = K_0$ respectively. Here K_0 is the primary value of anisotropy constant in FePS$_3$.

tice magnetization saturation of an AFM material, this suggests that any AFM material with anisotropy energy comparable to that of FePS$_3$ (of order one meV) may be a promising alternative candidate for realizing strong coupling between a surface-plasmon-phonon polariton in a TI and magnon polaritons in an AFM. Possible alternative AFM material that are promising include: L1$_2$ IrMn$_3$ ($\Delta = 6.81$ meV) [68], Na$_4$IrO$_4$ ($\Delta = 5.4$ meV) [69], and Cr–trihalide Janus monolayers with applied strain up to

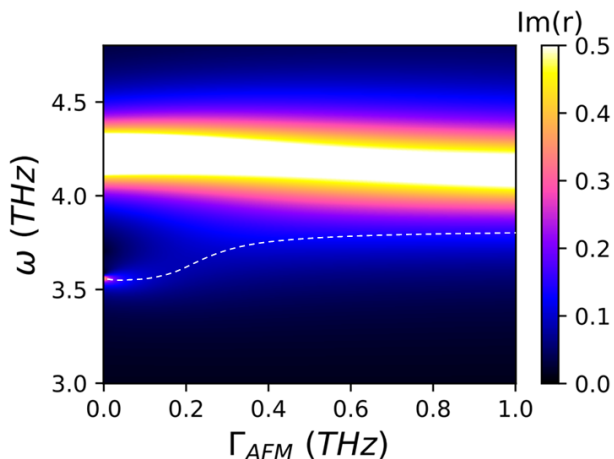5% (giving $\Delta = 3.77\ meV$ for Cl_3-Cr_2-I_3 monolayer) [70].

FIG. 11. Mode energies of a SDPP-MP in a Sb_2Te_3/$FePS_3$ bilayer structure with Sb_2Te_3 thickness $d_{TI} = 500\ nm$ and a half-infinite $FePS_3$ as a function of the scattering loss rate in the AFM. The dashed white line represents the evolution of lower mode v.s. Γ_{AFM}. This calculation is performed at fixed in plane wave vector $k_x = 0.03 \times 10^5\ cm^{-1}$, which is at the anti-crossing point.

Finally, in the calculations presented thus far we have assumed that the scattering loss rate in the $FePS_3$ AFM is $\Gamma_{AFM} = 0.035\ THz$, which is a value taken from Ref [21]. This scattering rate parameter depends largely on crystalline and interface quality, which are specific to individual samples. We therefore consider the effect of changing scattering loss rates in the AFM material on the strength of the coupling between the TI and AFM. In Fig. 11, we plot the mode energies of SDPP-MPs in the TI/AFM structure shown in Fig.1 using $d_{TI} = 500\ nm$ and a very thick (half-infinite) AFM layer. We plot the mode energies near $\omega = 3.7\ THz$ as a function of the scattering loss rate in the AFM material for a fixed in-plane wave vector $k_x = 0.03 \times 10^5\ cm^{-1}$. In other words, we focus on the anti-crossing point in the dispersion spectrum. When the scattering loss rate of the AFM material is low (left side of Fig. 11), we observe two distinct modes at $3.5\ THz$ and $4.2\ THz$. This is the signature of the interaction between the surface DPPPs in the TI and the MPs in the AFM layer that results in the anti-crossing splitting. The two distinct modes disappear when the scattering loss rate exceeds 0.2 THz. The loss of distinct modes (collapse of the anti-crossing) occurs when the loss rate in the AFM exceeds the coupling strength. $\Gamma_{AFM} = 0.2\ THz$ therefore provides a benchmark for the AFM quality required to experimentally realize observable strong coupling between a TI and an AFM. We note that the scattering loss rates of AFM materials are typically in the GHz range, which is well below this threshold.

IV. CONCLUSION

We have studied strong coupling between surface Dirac plasmon-phonon-polaritons in a TI thin film and magnon polaritons in an AFM material using a numerical semi-classical approach. Our results show that spectral signatures of strong coupling, specifically hybridized surface Dirac plasmon-phonon-magnon polaritons with cooperativity factor $C > 1$, can emerge in a Sb_2Te_3 / $FePS_3$ heterostructure when (a) the thickness of the AFM material ($FePS_3$) is sufficiently large (about $\approx 3000\ nm$), (b) the thickness of the TI thin film (Sb_2Te_3) is about 500 nm, and (c) the quality of the AFM material is sufficiently high that the scattering loss rate does not exceed 0.1 THz. All of these structural and materials parameters should be experimentally realizable. Equally importantly, our analysis as a function of various structural parameters allows us to understand the physical interactions that underly the coupling. For example, our analysis reveals the important role of phonons in the TI as a mediator of the interaction between the TI and AFM. Because of the important role played by phonons, and in particular the ability to tune the energy of the surface Dirac plasmon phonon polariton mode with the thickness of the TI, TIs have a significant advantage over 2D materials such as graphene for achieving strong interactions between surface Dirac plasmons and magnon polaritons. Finally, our calculations suggest that any 2D van der Waals and other types of AFM materials with a large anisotropy constant could be a viable choice for realizing strong coupling in a TI / AFM hybrid material.

Appendix A: Magnetic susceptibility of XPS_3 (X = Mn, Fe, Co, Ni)

In this appendix, we derive the frequency dependent magnetic susceptibility for 2D antiferromagnetic materials in the family XPS_3 (X = Mn, Fe, Co, Ni), which includes the $FePS_3$ studied in the main text. These materials are van der Waals magnets that form layered structures weakly bound by van der Waals forces. Figure 12 shows the layered magnetic structure of $FePS_3$ established by only the Fe atoms. Within each layer, the Fe atoms arrange in a honeycomb-like lattice structure with opposite spin moments. We consider in this work the $FePS_3$ magnetic structure with zigzag AFM phase, but our method presented in this section can be applied to the general case of any 2D antiferromagnetic material with different AFM phases.
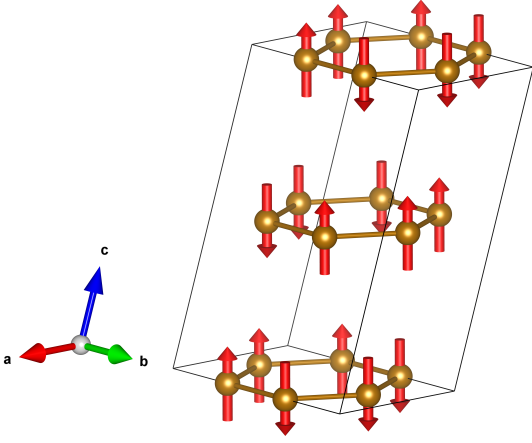
FIG. 12. The layered magnetic lattice of FePS$_3$ formed by Fe atoms. The arrows indicate direction of spin moment with Zigzag AFM phases investigated in this work. This figure is plotted by using VESTA software [71]

Due to the small value of the interlayer exchange interaction J' in comparison to the intralayer exchange interaction J_i ($i = 1, 2, 3$), these AFM are, to a very good approximation, quasi-two dimensional magnets even in the bulk. The magnon dynamics in FePS$_3$ can therefore be considered by investigating a quasi-2D honeycomb structure of Fe atoms in which the magnetic interactions within the lattice are described via a Heisenberg Hamiltonian [26]:

$$H = \sum_{i,j \neq i} 2J_{i,j} \boldsymbol{S}_i \cdot \boldsymbol{S}_j + \Delta \sum_i (S_i^z)^2 - \gamma\hbar \sum_i h_0^z S_i^z + \gamma\hbar \sum_i \boldsymbol{h} \cdot \boldsymbol{S}_i \tag{A1}$$

where γ is the gyromagnetic ratio, $\hbar$ is Planck's constant, h_0^z is an external static magnetic field applied to the lattice along the z-direction, $\boldsymbol{h}$ is a driven magnetic field, $\boldsymbol{S_i}$ is the spin operator, J_{ij} is the exchange energy of the interaction between site $i^{t}h$ and j^{th}, and Δ is the single atom anisotropy energy. Table II presents the spin-spin interaction parameters of the AFM materials used in this study.

TABLE II. The spin-spin interaction parameters of the 2D AFM materials used in this work.

Materials	J_1 (meV)	J_2 (meV)	J_3 (meV)	J' (meV)	Δ (meV)
FePS$_3$ [26]	1.49	0.04	-0.6	-0.0073	-3.6
NiPS$_3$[49]	3.8	-0.2	-13.8	N/A	-0.3
MnPS$_3$[49]	-1.54	-0.14	-0.36	0.0019	-0.0086

Considering a uniform precession of spin moments under the driven magnetic field $\boldsymbol{h}$, we use a macrospin approximation with the uniform sublattice magnetizations in sublattice A and B, given respectively by $\boldsymbol{M}_{A,B} = \gamma\hbar N \boldsymbol{S}_{A,B}$, where N is the number of spins per unit volume and $\boldsymbol{S}_{A,B}$ is the spin in units of $\hbar$ ($S = |\boldsymbol{S}_{A,B}| = 2$ in the case of Fe atom). We note that in the XPS$_3$ AFM family, one needs to consider the exchange interactions between two magnetic moments up to the third nearest neighbor $J_{i=1,2,3}$ associated with the vectors joining nearest $\alpha_{i=1,2,3}$, second nearest $\beta_{i=1,2,3}$, and third nearest $\gamma_{i=1,2,3}$ neighboring Fe atoms as indicated in the Fig 13 [72]. Using the Hamiltonian A1, one obtains the energy per unit volume:

$$E = \xi \left(M_A^2 + M_B^2 \right) + \eta \boldsymbol{M}_A \cdot \boldsymbol{M}_B + \vartheta \left[(M_A^z)^2 + (M_B^z)^2 \right] - h_0^z (M_A^z + M_B^z) - \boldsymbol{h} \cdot (\boldsymbol{M}_A + \boldsymbol{M}_B) \tag{A2}$$

where $\xi = \frac{2(J_1+J_2)S}{\gamma\hbar M_0}$, $\eta = \frac{2(J_1+4J_2+3J_3)S}{\gamma\hbar M_0}$, $\vartheta = \frac{\Delta S}{\gamma\hbar M_0}$, and M_0 is the magnetization of one sublattice per volume.

Suppose a transverse magnetic field $\boldsymbol{h} = \boldsymbol{h}(t) = (h_x, h_y, 0)\, e^{-i\omega t}$ drives the spin dynamics in the lattice governed by the Landau-Lifshitz equation

$$\frac{d}{dt} \boldsymbol{M}_{A,B} = \frac{g\mu_B}{\hbar} \boldsymbol{M}_{A,B} \times \boldsymbol{F}_{A,B}^{eff} \qquad (A3)$$

where $\boldsymbol{F}_{A,B}^{eff} = -\boldsymbol{\nabla}_{A,B} E\left(\boldsymbol{M}_{A,B}\right)$ is the effective force acting on the A (B) spin sublattice and the magnetic moment $\boldsymbol{M}_{A,B} = m_{A,B}^x e^{-i\omega t}\hat{x} + m_{A,B}^y e^{-i\omega t}\hat{y} + M_{A,B}^z \hat{z}$.

In this case one has

$$\frac{d}{dt} \boldsymbol{M}_{A,B} = -i\omega e^{-i\omega t} \begin{pmatrix} m_{A,B}^x \\ m_{A,B}^y \\ 0 \end{pmatrix} \qquad (A4)$$

and

$$\boldsymbol{F}_{A,B}^{eff} = - \begin{pmatrix} 2\xi m_{A,B}^x e^{-i\omega t} + \eta m_{B,A}^x e^{-i\omega t} - h_x e^{-i\omega t} \\ 2\xi m_{A,B}^y e^{-i\omega t} + \eta m_{B,A}^y e^{-i\omega t} - h_y e^{-i\omega t} \\ 2\left(\xi + \vartheta\right) M_{A,B}^z + \eta M_{B,A}^z - h_0^z \end{pmatrix} \qquad (A5)$$

leading to a set of equations of transverse motion for the two-spin sublattices A and B:

$$\begin{pmatrix} m_A^x \\ m_A^y \\ m_B^x \\ m_B^y \end{pmatrix} = D^{-1} C \begin{pmatrix} h_y \\ h_x \\ h_y \\ h_x \end{pmatrix} \qquad (A6)$$

where

$$D = \begin{bmatrix} i\omega & -\gamma\left(2\vartheta M_A^z + \eta M_B^z - h_0^z\right) & 0 & \gamma\eta M_A^z \\ \gamma\left(2\vartheta M_A^z + \eta M_B^z - h_0^z\right) & i\omega & -\gamma\eta M_A^z & 0 \\ 0 & \gamma\eta M_B^z & i\omega & -\gamma\left(2\vartheta M_B^z + \eta M_A^z - h_0^z\right) \\ -\gamma\eta M_B^z & 0 & \gamma\left(2\vartheta M_B^z + \eta M_A^z - h_0^z\right) & i\omega \end{bmatrix} \qquad (A7)$$

and $C = diag\left(\gamma M_A^z, -\gamma M_A^z, \gamma M_B^z, -\gamma M_B^z\right)$. The determinant of matrix D (Eqn. A7) is given by:

$$det|D| = \omega^4 - 2\gamma^2 \left[4\vartheta^2 \left(M_0^z\right)^2 - 4\eta\vartheta \left(M_0^z\right)^2 + \left(h_0^z\right)^2\right]\omega^2 + \gamma^4 \left[4\vartheta^2 \left(M_0^z\right)^2 - 4\eta\vartheta \left(M_0^z\right)^2 - \left(h_0^z\right)^2\right]^2 \qquad (A8)$$

$$= \left[\omega^2 - \gamma^2 \left(\sqrt{4\vartheta^2 \left(M_0^z\right)^2 - 4\eta\vartheta \left(M_0^z\right)^2} + h_0^z\right)^2\right]\left[\omega^2 - \gamma^2 \left(\sqrt{4\vartheta^2 \left(M_0^z\right)^2 - 4\eta\vartheta \left(M_0^z\right)^2} - h_0^z\right)^2\right] \qquad (A9)$$

$$= \left[4\gamma^2\vartheta^2 \left(M_0^z\right)^2 - 4\gamma^2\eta\vartheta \left(M_0^z\right)^2 - \left(\omega - \gamma h_0^z\right)^2\right]\left[4\gamma^2\vartheta^2 \left(M_0^z\right)^2 - 4\gamma^2\eta\vartheta \left(M_0^z\right)^2 - \left(\omega + \gamma h_0^z\right)^2\right] \qquad (A10)$$

$$= \left[\Omega_0^2 - \left(\omega - \gamma h_0^z\right)^2\right]\left[\Omega_0^2 - \left(\omega + \gamma h_0^z\right)^2\right] \qquad (A11)$$

Here we have used $\Omega_0^2 = 4\gamma^2\vartheta^2 \left(M_0^z\right)^2 - 4\gamma^2\eta\vartheta \left(M_0^z\right)^2$.

We now define a total magnetic moment as

$$\boldsymbol{M}_t = \begin{pmatrix} m_A^x + m_B^x \\ m_A^y + m_B^y \end{pmatrix} = \begin{pmatrix} \chi^{xx} & \chi^{xy} \\ \chi^{yx} & \chi^{yy} \end{pmatrix}\begin{pmatrix} h_x \\ h_y \end{pmatrix} \qquad (A12)$$

where $\begin{pmatrix} \chi^{xx} & \chi^{xy} \\ \chi^{yx} & \chi^{yy} \end{pmatrix}$ is the magnetic susceptibility tensor.

Solving Eq.A6 within the linear approximation $M_A^z = -M_B^z = M_0^z$, one obtains the magnetic susceptibility tensor given by

$$\chi^{xx} = \frac{4\gamma^2\vartheta \left(M_0^z\right)^2 \left[\omega^2 - \Omega_0^2 + \left(\gamma h_0^z\right)^2\right]}{det|D|} \qquad (A13)$$

$$\chi^{xy} = \frac{8i\gamma^3\vartheta \left(M_0^z\right)^2 h_0^z\omega}{det|D|} \qquad (A14)$$

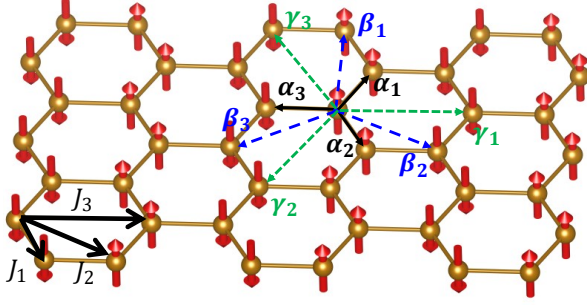with $\chi^{xx} = \chi^{yy}$ and $\chi^{xy} = -\chi^{yx}$.

FIG. 13. The quasi-2D magnetic lattice of FePS$_3$ formed by Fe atoms. The arrows indicate the direction of the spin moments with Zigzag AFM phases investigated in this work.

If we call

$$H_e = \eta M_0 = \frac{2\left(J_1 + 4J_2 + 3J_3\right)S}{\gamma\hbar} \quad \text{(A15)}$$

$$H_a = 2\vartheta M_0 = \frac{2\Delta S}{\gamma\hbar} \quad \text{(A16)}$$

the, respectively, effective exchange field and effective anisotropy field, then in the case of vanishing external magnetic field $h_0^z = 0$, one obtains

$$\chi^{xx} = \chi^{yy} = \frac{2\gamma^2 H_a M_0}{\Omega_0^2 - \omega^2} \quad \text{(A17)}$$

$$\chi^{xy} = \chi^{yx} = 0 \quad \text{(A18)}$$

where we have used $M_0^z \approx M_0$ and $\Omega_0^2 = \gamma^2\left(H_a^2 - 2H_e H_a\right)$ is the antiferromagnetic resonance frequency or zero-wave vector magnon frequency in the antiferromagnetic material. In a system with non-vanishing scattering loss rate, one has

$$\chi^{xx} = \chi^{yy} = \frac{2\gamma^2 H_a M_0}{\Omega_0^2 - \left(\omega + i/\tau_{mag}\right)^2} \quad \text{(A19)}$$

$$\chi^{xy} = \chi^{yx} = 0 \quad \text{(A20)}$$

with τ_{mag} the relaxation time of the magnon.

The antiferromagnetic resonance frequency or zero-wave magnon frequency in the FePS$_3$ material $\Omega_0^{FePS_3} = 3.7\ THz$ [26, 51] and its magnetization $M_0^{FePS_3} \approx 830\ (G)$ [73]. In order to obtain the H_a effective anisotropy field of FePS$_3$ we note that this effective anisotropy field is proportional to the magnitudes of the anisotropy energy Δ, and the spin S of the antiferromagnetic material, which are respective $\Delta = 3.6\ meV$ taken

from reference [26] and $S = 2$ in FePS$_3$. For comparison, those values in MnF$_2$ are, respectively, about 0.0024 meV and 2.5, which correspond to the effective anisotropy field $H_a^{MnF_2} = 8.2\ kOe$ [74]. We therefore estimate the value for the effective anisotropy field in FePS$_3$ to be about $H_a^{FePS_3} = 9840\ kOe$ and use this value in the calculations reported in the main text.

Appendix B: Global scattering matrix

We now present in detail the so-called global scattering matrix method used to solve Maxwell's equations to obtain the dispersion relations studied in the main text. This method is similar to the Green's function technique used to investigate scattering for a propagating wave in a multi-layered structure by an evaluation of the S-scattering matrix computed from the scattering path operator and has been successfully employed to study electric and spin transport in several system [61–63]. Here we adopt this robust technique to the optical system studied in this article.
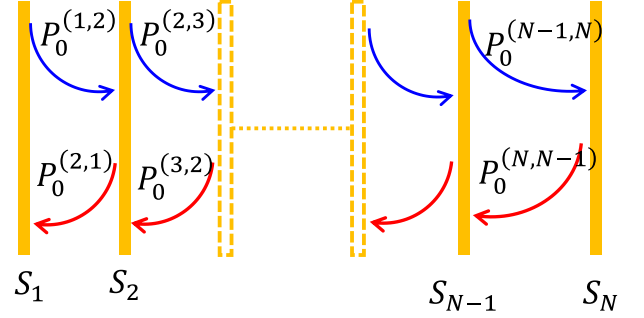

FIG. 14. Schematic of a heterostructure composed of N interface with interfacial scattering matrix S_i and propagation matrix P_0^{ij} describing a scattering process in this structure.

Consider a heterostructure with N interface as shown in Fig 14. We denote the z-axis as the growth direction of the structure. The dimension of the heterostructure along the y-axis is infinite and along the x-direction it is finite with a width W. Assuming that an EM wave beam is incident from the left-hand side of the structure with the direction of propagation to parallel to the x-z plane, within the mth layer the electric field $\boldsymbol{E}_m = \left(E_{x,m}, E_{y,m}, E_{z,m}\right)$ and the magnetic field $\boldsymbol{H}_m = \left(H_{x,m}, H_{y,m}, H_{z,m}\right)$ components of a monochromatic electromagnetic wave that is a solution of Maxwell's equations propagating along the z direction take the general form:

$$\boldsymbol{E}_m = e^{i(k_{x,m}x-\omega t)} \begin{bmatrix} e^{ik_{z,m}z} & 0 & e^{-ik_{z,m}z} & 0 \\ 0 & e^{ik_{z,m}z} & 0 & e^{-ik_{z,m}z} \\ -\frac{\varepsilon_m^{\parallel} k_{x,m}}{\varepsilon_m^{\perp} k_{z,m}} e^{ik_{z,m}z} & 0 & \frac{\varepsilon_m^{\parallel} k_{x,m}}{\varepsilon_m^{\perp} k_{z,m}} e^{-ik_{z,m}z} & 0 \end{bmatrix} \begin{pmatrix} A_{x,m} \\ A_{y,m} \\ B_{x,m} \\ B_{y,m} \end{pmatrix} \tag{B1}$$

$$\boldsymbol{H}_m = \frac{e^{i(k_{x,m}x-\omega t)}}{\mu_0 \mu_m} \begin{bmatrix} 0 & -\frac{k_{z,m}}{\omega} e^{ik_{z,m}z} & 0 & \frac{k_{z,m}}{\omega} e^{-ik_{z,m}z} \\ \frac{1}{\omega k_{z,m}} \left(\frac{\varepsilon_m^{\parallel}}{\varepsilon_m^{\perp}} k_{x,m}^2 + k_{z,m}^2 \right) e^{ik_{z,m}z} & 0 & -\frac{1}{\omega k_{z,m}} \left(\frac{\varepsilon_m^{\parallel}}{\varepsilon_m^{\perp}} k_{x,m}^2 + k_{z,m}^2 \right) e^{-ik_{z,m}z} & 0 \\ 0 & \frac{k_{x,m}}{\omega} e^{ik_{z,m}z} & 0 & \frac{k_{x,m}}{\omega} e^{-ik_{z,m}z} \end{bmatrix} \begin{pmatrix} A_{x,m} \\ A_{y,m} \\ B_{x,m} \\ B_{y,m} \end{pmatrix} \tag{B2}$$

where $A_{(x,y),m}$ and $B_{(x,y),m}$ are the amplitudes of the x- and y- components of the forward- and backward-propagating EM waves, respectively; ω is the frequency of the EM wave; $k_{x,m}$ and $k_{z,m}$ are the x- and z-components of the wave vector of the EM wave within the mth layer; and x and z are the coordinates along the x- and z- directions.

At the mth interface, the amplitudes of the EM wave should satisfy the standard boundary conditions [75, 76]:

$$\boldsymbol{n} \times (\boldsymbol{E}_{m+1} - \boldsymbol{E}_m)|_m = 0 \tag{B3}$$
$$\boldsymbol{n} \times (\boldsymbol{H}_{m+1} - \boldsymbol{H}_m)|_m = \boldsymbol{J}_m \tag{B4}$$

where

$$\boldsymbol{n} = \begin{pmatrix} 0 \\ 0 \\ 1 \end{pmatrix}, \quad \boldsymbol{J}_m = \sigma_m \boldsymbol{E}_{m+1}, \quad \sigma_m = \begin{pmatrix} \sigma_m^{xx} & \sigma_m^{xy} \\ \sigma_m^{yx} & \sigma_m^{yy} \end{pmatrix} \tag{B5}$$

Here σ_m is the optical conductivity tensor of the corresponding two-dimensional carrier gas at the mth-interface. Substituting Eqs. B1 and B2 into Eqs. B3 and B4, one obtains

$$\begin{pmatrix} A_{x,m} \\ A_{y,m} \\ B_{x,m} \\ B_{y,m} \end{pmatrix} = I_m \begin{pmatrix} A_{x,m+1} \\ A_{y,m+1} \\ B_{x,m+1} \\ B_{y,m+1} \end{pmatrix} \tag{B6}$$

where I_m is an interface matrix that relates the amplitudes of the EM wave in the adjacent m^{th} and $(m+1)^{th}$ layers. If we define:

$$U = \begin{pmatrix} 1 & 0 & 1 & 0 \\ 0 & 1 & 0 & 1 \end{pmatrix}, \quad V = \begin{pmatrix} 1 & 0 & 0 \\ 0 & 1 & 0 \end{pmatrix} \tag{B7}$$

then the interface matrix I_m will read:

$$I_m = \begin{pmatrix} I_m^{11} & I_m^{12} \\ I_m^{21} & I_m^{22} \end{pmatrix} = \begin{pmatrix} U \\ L_m \end{pmatrix}^{-1} \begin{pmatrix} U \\ R_m \end{pmatrix} \tag{B8}$$

where I_m^{ij} $(i,j = 1, 2)$ are 2×2 matrices,

$$L_m = \frac{V}{\mu_0 \mu_m} \begin{pmatrix} 0 & -\frac{k_{z,m}}{\omega} & 0 & \frac{k_{z,m}}{\omega} \\ \frac{(\varepsilon_m^{\parallel} k_{x,m}^2 + \varepsilon_m^{\perp} k_{z,m}^2)}{\varepsilon_m^{\perp} \omega k_{z,m}} & 0 & -\frac{(\varepsilon_m^{\parallel} k_{x,m}^2 + \varepsilon_m^{\perp} k_{z,m}^2)}{\varepsilon_m^{\perp} \omega k_{z,m}} & 0 \\ 0 & \frac{k_{x,m}}{\omega} & 0 & \frac{k_{x,m}}{\omega} \end{pmatrix} \tag{B9}$$

and

$$R_m = \frac{V}{\mu_0 \mu_{m+1}} \begin{pmatrix} 0 & -\frac{k_{z,m+1}}{\omega} & 0 & \frac{k_{z,m+1}}{\omega} \\ \frac{(\varepsilon_{m+1}^{\parallel} k_{x,m+1}^2 + \varepsilon_{m+1}^{\perp} k_{z,m+1}^2)}{\varepsilon_{m+1}^{\perp} \omega k_{z,m+1}} & 0 & -\frac{(\varepsilon_{m+1}^{\parallel} k_{x,m+1}^2 + \varepsilon_{m+1}^{\perp} k_{z,m+1}^2)}{\varepsilon_{m+1}^{\perp} \omega k_{z,m+1}} & 0 \\ 0 & \frac{k_{x,m+1}}{\omega} & 0 & \frac{k_{x,m+1}}{\omega} \end{pmatrix} + \begin{pmatrix} -\sigma_m^{yx} & -\sigma_m^{yy} & -\sigma_m^{yx} & -\sigma_m^{yy} \\ \sigma_m^{xx} & \sigma_m^{xy} & \sigma_m^{xx} & \sigma_m^{xy} \end{pmatrix} \tag{B10}$$

where $k_{z,m} = \sqrt{\frac{\omega^2}{c^2} \mu_m^{xx} \varepsilon_m^{\parallel} - \frac{\varepsilon_m^{\parallel}}{\varepsilon_m^{\perp}} k_{x,m}^2}$

We now define a scattering matrix at the mth interface

S_m such that:

This S_m is related to the interface matrix I_m by:

$$S_m = \begin{bmatrix} \left(I_m^{11}\right)^{-1} & -\left(I_m^{11}\right)^{-1} I_m^{12} \\ I_m^{21}\left(I_m^{11}\right)^{-1} & I_m^{22} - I_m^{21}\left(I_m^{11}\right)^{-1} I_m^{12} \end{bmatrix} \quad \text{(B12)}$$

A global scattering matrix S that describes the scattering processes of an EM wave propagating in a heterostructure composed of N-1 constituent materials is given by the super matrix form:

$$\begin{pmatrix} A_{x,m+1} \\ A_{y,m+1} \\ B_{x,m} \\ B_{y,m} \end{pmatrix} = S_m \begin{pmatrix} A_{x,m} \\ A_{y,m} \\ B_{x,m+1} \\ B_{y,m+1} \end{pmatrix} \quad \text{(B11)}$$

$$S = \begin{bmatrix} S_1^{-1} & -P_0^{(2,1)} & 0 & 0 & \ldots & 0 & 0 \\ -P_0^{(1,2)} & S_2^{-1} & -P_0^{(3,2)} & 0 & \ldots & 0 & 0 \\ 0 & -P_0^{(2,3)} & S_3^{-1} & -P_0^{(4,3)} & \ldots & 0 & 0 \\ 0 & 0 & -P_0^{(3,4)} & S_4^{-1} & \ldots & 0 & 0 \\ \vdots & \vdots & \vdots & \vdots & \ddots & \vdots & \vdots \\ 0 & 0 & 0 & 0 & \ldots & S_{N-1}^{-1} & -P_0^{(N,N-1)} \\ 0 & 0 & 0 & 0 & \ldots & -P_0^{(N-1,N)} & S_N^{-1} \end{bmatrix}^{-1} \quad \text{(B13)}$$

Here the propagation matrices for an EM wave propagat-

ing between the mth and $(m+1)^{th}$ interfaces takes the form

$$P_0^{m,m+1} = \begin{pmatrix} e^{ik_{z,m+1}d_{m+1}} & 0 & 0 & 0 \\ 0 & e^{ik_{z,m+1}d_{m+1}} & 0 & 0 \\ 0 & 0 & 0 & 0 \\ 0 & 0 & 0 & 0 \end{pmatrix}, \quad P_0^{m+1,m} = \begin{pmatrix} 0 & 0 & 0 & 0 \\ 0 & 0 & 0 & 0 \\ 0 & 0 & e^{ik_{z,m+1}d_{m+1}} & 0 \\ 0 & 0 & 0 & e^{ik_{z,m+1}d_{m+1}} \end{pmatrix} \quad \text{(B14)}$$

and S_m^{-1} $(m = 1 \div N)$ is the inversion of the matrix S_m given in Eq. B12. The global scattering matrix S can then be written in terms of

$$S = \begin{pmatrix} S_{11} & S_{12} & \cdots & S_{1N} \\ S_{21} & S_{22} & \cdots & S_{2N} \\ \vdots & \vdots & \ddots & \vdots \\ S_{N1} & S_{N2} & \cdots & S_{NN} \end{pmatrix} \quad \text{(B15)}$$

where S_{ij} $(i,j = 1 \div N)$ is a 4×4 block matrix element of S that describes the scattering event of the EM wave that starts at the jth interface and ends up at the ith interface. In particular

$$S_{ij} = \begin{pmatrix} S_{ij}^{11} & S_{ij}^{12} \\ S_{ij}^{21} & S_{ij}^{22} \end{pmatrix} = \begin{pmatrix} t_{ij} & r'_{ij} \\ r_{ij} & t'_{ij} \end{pmatrix} \quad \text{(B16)}$$

where S_{ij}^{11} and S_{ij}^{21} are the block matrices giving the

transmission t_{ij} and reflection r_{ij} coefficients associated with the incident wave propagating along the +z direction . In contrast, S_{ij}^{22} and S_{ij}^{12} (t'_{ij} and r'_{ij}) correspond to the incident wave propagating along the -z direction. For instance, the reflection coefficient of the entire system with N interfaces is derived from the S_{11}^{21} element whereas the transmission coefficient of the entire system is obtained from the S_{N1}^{11} element. In summary, using a global scattering matrix one can compute the optical response of the entire structure because the global scattering matrix captures what happen at each interface and within each layer of the structure. In the main text, we have calculated the imaginary part of S_{11}^{21} and used it to reveal the dispersion relations for the surface plasmon-phonon-magnon polariton in a TI/AFM structure.

[1] P. H. Siegel, Thz technology: An overview, Terahertz Sensing Technology: Volume 1: Electronic Devices and Advanced Systems Technology , 1 (2003).

[2] A. Y. Pawar, D. D. Sonawane, K. B. Erande, and D. V. Derle, Terahertz technology and its applications, Drug invention today **5**, 157 (2013).

[3] J. Walowski and M. Münzenberg, Perspective: Ultrafast magnetism and thz spintronics, Journal of Applied Physics **120**, 140901 (2016).

[4] K. Zaytsev, I. Dolganova, N. Chernomyrdin, G. Katyba, A. Gavdush, O. Cherkasova, G. Komandin, M. Shchedrina, A. Khodan, D. Ponomarev, *et al.*, The progress and perspectives of terahertz technology for diagnosis of neoplasms: a review, Journal of Optics **22**, 013001 (2019).

[5] T. Amini, F. Jahangiri, Z. Ameri, and M. A. Hemmatian, A review of feasible applications of thz waves in medical diagnostics and treatments, Journal of Lasers in Medical Sciences **12** (2021).

[6] N. M. Burford and M. O. El-Shenawee, Review of terahertz photoconductive antenna technology, Optical Engineering **56**, 010901 (2017).

[7] T. Dang, J. Hawecker, E. Rongione, G. Baez Flores, D. To, J. Rojas-Sanchez, H. Nong, J. Mangeney, J. Tignon, F. Godel, *et al.*, Ultrafast spin-currents and charge conversion at 3 d-5 d interfaces probed by time-domain terahertz spectroscopy, Applied Physics Reviews **7**, 041409 (2020).

[8] E. T. Papaioannou and R. Beigang, Thz spintronic emitters: a review on achievements and future challenges, Nanophotonics **10**, 1243 (2021).

[9] W. Wu, C. Yaw Ameyaw, M. F. Doty, and M. B. Jungfleisch, Principles of spintronic thz emitters, Journal of Applied Physics **130**, 091101 (2021).

[10] T. S. Seifert, L. Cheng, Z. Wei, T. Kampfrath, and J. Qi, Spintronic sources of ultrashort terahertz electromagnetic pulses (2022).

[11] P. Di Pietro, M. Ortolani, O. Limaj, A. Di Gaspare, V. Giliberti, F. Giorgianni, M. Brahlek, N. Bansal, N. Koirala, S. Oh, *et al.*, Observation of dirac plasmons in a topological insulator, Nature nanotechnology **8**, 556 (2013).

[12] T. Stauber, G. Gómez-Santos, and L. Brey, Plasmonics in topological insulators: Spin–charge separation, the influence of the inversion layer, and phonon–plasmon coupling, Acs Photonics **4**, 2978 (2017).

[13] T. Ginley, Y. Wang, Z. Wang, and S. Law, Dirac plasmons and beyond: the past, present, and future of plasmonics in 3d topological insulators, MRS Communications **8**, 782 (2018).

[14] P. Di Pietro, N. Adhlakha, F. Piccirilli, A. Di Gaspare, J. Moon, S. Oh, S. Di Mitri, S. Spampinati, A. Perucchi, and S. Lupi, Terahertz tuning of dirac plasmons in bi$_2$se$_3$ topological insulator, Phys. Rev. Lett. **124**, 226403 (2020).

[15] M. B. Jungfleisch, W. Zhang, and A. Hoffmann, Perspectives of antiferromagnetic spintronics, Physics Letters A **382**, 865 (2018).

[16] M. Gibertini, M. Koperski, A. F. Morpurgo, and K. S. Novoselov, Magnetic 2d materials and heterostructures, Nature nanotechnology **14**, 408 (2019).

[17] B. Huang, M. A. McGuire, A. F. May, D. Xiao, P. Jarillo-Herrero, and X. Xu, Emergent phenomena and proximity effects in two-dimensional magnets and heterostructures, Nature Materials **19**, 1276 (2020).

[18] X.-X. Zhang, L. Li, D. Weber, J. Goldberger, K. F. Mak, and J. Shan, Gate-tunable spin waves in antiferromagnetic atomic bilayers, Nature materials **19**, 838 (2020).

[19] S. Yang, T. Zhang, and C. Jiang, van der waals magnets: material family, detection and modulation of magnetism, and perspective in spintronics, Advanced Science **8**, 2002488 (2021).

[20] X. Jiang, Q. Liu, J. Xing, N. Liu, Y. Guo, Z. Liu, and J. Zhao, Recent progress on 2d magnets: Fundamental mechanism, structural design and modification, Applied Physics Reviews **8**, 031305 (2021).

[21] Q. Zhang, M. Ozerov, E. V. Boström, J. Cui, N. Suri, Q. Jiang, C. Wang, F. Wu, K. Hwangbo, J.-H. Chu, *et al.*, Coherent strong-coupling of terahertz magnons and phonons in a van der waals antiferromagnetic insulator, arXiv preprint arXiv:2108.11619 (2021).

[22] C. A. Belvin, E. Baldini, I. O. Ozel, D. Mao, H. C. Po, C. J. Allington, S. Son, B. H. Kim, J. Kim, I. Hwang, *et al.*, Exciton-driven antiferromagnetic metal in a correlated van der waals insulator, Nature communications **12**, 1 (2021).

[23] J. Han, P. Zhang, J. T. Hou, S. A. Siddiqui, and L. Liu, Mutual control of coherent spin waves and magnetic domain walls in a magnonic device, Science **366**, 1121 (2019).

[24] H. Fulara, M. Zahedinejad, R. Khymyn, A. Awad, S. Muralidhar, M. Dvornik, and J. Åkerman, Spin-orbit torque–driven propagating spin waves, Science advances **5**, eaax8467 (2019).

[25] Y. Wang, D. Zhu, Y. Yang, K. Lee, R. Mishra, G. Go, S.-H. Oh, D.-H. Kim, K. Cai, E. Liu, *et al.*, Magnetization switching by magnon-mediated spin torque through an antiferromagnetic insulator, Science **366**, 1125 (2019).

[26] S. Liu, A. Granados del Águila, D. Bhowmick, C. K. Gan, T. Thu Ha Do, M. A. Prosnikov, D. Sedmidubský, Z. Sofer, P. C. M. Christianen, P. Sengupta, and Q. Xiong, Direct observation of magnon-phonon strong coupling in two-dimensional antiferromagnet at high magnetic fields, Phys. Rev. Lett. **127**, 097401 (2021).

[27] H. Yuan and X. Wang, Magnon-photon coupling in antiferromagnets, Applied Physics Letters **110**, 082403 (2017).

[28] I. A. Golovchanskiy, N. N. Abramov, V. S. Stolyarov, M. Weides, V. V. Ryazanov, A. A. Golubov, A. V. Ustinov, and M. Y. Kupriyanov, Ultrastrong photon-to-magnon coupling in multilayered heterostructures involving superconducting coherence via ferromagnetic layers, Science advances **7**, eabe8638 (2021).

[29] Y. Xiao, X. H. Yan, L. H. Bai, H. Guo, C. M. Hu, and K. Xia, Magnon photon coupling for magnetization antiparallel to the magnetic field, Phys. Rev. B **103**, 104432 (2021).

[30] J. Henriques, T. Antão, and N. Peres, Laser induced enhanced coupling between photons and squeezed magnons in antiferromagnets, Journal of Physics: Condensed Matter **34**, 245802 (2022).

[31] J. Pitarke, V. Silkin, E. Chulkov, and P. Echenique, Theory of surface plasmons and surface-plasmon polaritons, Reports on progress in physics **70**, 1 (2006).

[32] J. Zhang, L. Zhang, and W. Xu, Surface plasmon polaritons: physics and applications, Journal of Physics D: Applied Physics **45**, 113001 (2012).

[33] P. Törmä and W. L. Barnes, Strong coupling between surface plasmon polaritons and emitters: a review, Reports on Progress in Physics **78**, 013901 (2014).

[34] T. Stauber, G. Gómez-Santos, and L. Brey, Spin-charge

separation of plasmonic excitations in thin topological insulators, Phys. Rev. B **88**, 205427 (2013).

[35] J. Qi, H. Liu, and X. C. Xie, Surface plasmon polaritons in topological insulators, Phys. Rev. B **89**, 155420 (2014).

[36] Y. Deshko, L. Krusin-Elbaum, V. Menon, A. Khanikaev, and J. Trevino, Surface plasmon polaritons in topological insulator nano-films and superlattices, Optics Express **24**, 7398 (2016).

[37] Z. Wang, T. P. Ginley, S. V. Mambakkam, G. Chandan, Y. Zhang, C. Ni, and S. Law, Plasmon coupling in topological insulator multilayers, Phys. Rev. Materials **4**, 115202 (2020).

[38] N. S. Almeida and D. L. Mills, Dynamical response of antiferromagnets in an oblique magnetic field: Application to surface magnons, Phys. Rev. B **37**, 3400 (1988).

[39] T. Dumelow and M. C. Oliveros, Continuum model of confined magnon polaritons in superlattices of antiferromagnets, Phys. Rev. B **55**, 994 (1997).

[40] J. Sloan, N. Rivera, J. D. Joannopoulos, I. Kaminer, and M. Soljačić, Controlling spins with surface magnon polaritons, Phys. Rev. B **100**, 235453 (2019).

[41] R. Macêdo and R. E. Camley, Engineering terahertz surface magnon-polaritons in hyperbolic antiferromagnets, Phys. Rev. B **99**, 014437 (2019).

[42] M. Vasconcelos, M. Cottam, and D. Anselmo, Magnon-polaritons in graphene/gyromagnetic slab heterostructures, Journal of Physics: Condensed Matter **33**, 055801 (2020).

[43] S. Hao, S. Fu, S. Zhou, and X.-Z. Wang, Dyakonov surface magnons and magnon polaritons, Physical Review B **104**, 045407 (2021).

[44] Y. V. Bludov, J. N. Gomes, G. d. A. Farias, J. Fernández-Rossier, M. Vasilevskiy, and N. M. Peres, Hybrid plasmon-magnon polaritons in graphene-antiferromagnet heterostructures, 2D Materials **6**, 045003 (2019).

[45] A. M. Pikalov, A. V. Dorofeenko, and A. Granovsky, Plasmon–magnon interaction in the (graphene–antiferromagnetic insulator) system, JETP Letters **113**, 521 (2021).

[46] D. Q. To, Z. Wang, Y. Liu, W. Wu, M. B. Jungfleisch, J. Q. Xiao, J. M. O. Zide, S. Law, and M. F. Doty, Surface plasmon-phonon-magnon polariton in a topological insulator-antiferromagnetic bilayer structure, Phys. Rev. Materials **6**, 085201 (2022).

[47] A. Wildes, K. C. Rule, R. Bewley, M. Enderle, and T. J. Hicks, The magnon dynamics and spin exchange parameters of feps3, Journal of Physics: Condensed Matter **24**, 416004 (2012).

[48] D. Lançon, H. C. Walker, E. Ressouche, B. Ouladdiaf, K. C. Rule, G. J. McIntyre, T. J. Hicks, H. M. Rønnow, and A. R. Wildes, Magnetic structure and magnon dynamics of the quasi-two-dimensional antiferromagnet feps$_3$, Phys. Rev. B **94**, 214407 (2016).

[49] T. Olsen, Magnetic anisotropy and exchange interactions of two-dimensional feps3, nips3 and mnps3 from first principles calculations, Journal of Physics D: Applied Physics **54**, 314001 (2021).

[50] Y. Lee, S. Son, C. Kim, S. Kang, J. Shen, M. Kenzelmann, B. Delley, T. Savchenko, S. Parchenko, W. Na, *et al.*, Giant magnetic anisotropy in the atomically thin van der waals antiferromagnet feps3, arXiv preprint arXiv:2211.05381 (2022).

[51] A. McCreary, J. R. Simpson, T. T. Mai, R. D. McMichael, J. E. Douglas, N. Butch, C. Dennis, R. Valdés Aguilar, and A. R. Hight Walker, Quasi-two-dimensional magnon identification in antiferromagnetic FePs$_3$ via magneto-raman spectroscopy, Phys. Rev. B **101**, 064416 (2020).

[52] P. Forn-Díaz, L. Lamata, E. Rico, J. Kono, and E. Solano, Ultrastrong coupling regimes of light-matter interaction, Rev. Mod. Phys. **91**, 025005 (2019).

[53] A. Frisk Kockum, A. Miranowicz, S. De Liberato, S. Savasta, and F. Nori, Ultrastrong coupling between light and matter, Nature Reviews Physics **1**, 19 (2019).

[54] P. Sivarajah, A. Steinbacher, B. Dastrup, J. Lu, M. Xiang, W. Ren, S. Kamba, S. Cao, and K. A. Nelson, Thz-frequency magnon-phonon-polaritons in the collective strong-coupling regime, Journal of Applied Physics **125**, 213103 (2019).

[55] L. J. Zhu, D. C. Ralph, and R. A. Buhrman, Irrelevance of magnetic proximity effect to spin-orbit torques in heavy-metal/ferromagnet bilayers, Phys. Rev. B **98**, 134406 (2018).

[56] D. Q. To, Z. Wang, D. Q. Ho, R. Hu, W. Acuna, Y. Liu, G. W. Bryant, A. Janotti, J. M. O. Zide, S. Law, and M. F. Doty, Strong coupling between a topological insulator and a iii-v heterostructure at terahertz frequency, Phys. Rev. Materials **6**, 035201 (2022).

[57] W. Richter and C. Becker, A raman and far-infrared investigation of phonons in the rhombohedral v2–vi3 compounds bi2te3, bi2se3, sb2te3 and bi2 (te1- xsex) 3 (0¡ x¡ 1),(bi1- ysby) 2te3 (0¡ y¡ 1), physica status solidi (b) **84**, 619 (1977).

[58] A. Ghosh, M. Birowska, P. K. Ghose, M. Rybak, S. Maity, S. Ghosh, B. Das, S. Bera, S. Bhardwaj, S. Nandi, *et al.*, Anisotropic magnetodielectric coupling in layered antiferromagnetic feps _3, arXiv preprint arXiv:2208.02729 (2022).

[59] P. A. Joy and S. Vasudevan, Magnetism in the layered transition-metal thiophosphates mps$_3$ (m=mn, fe, and ni), Phys. Rev. B **46**, 5425 (1992).

[60] M. Subramanian, R. Shannon, B. Chai, M. Abraham, and M. Wintersgill, Dielectric constants of beo, mgo, and cao using the two-terminal method, Physics and chemistry of minerals **16**, 741 (1989).

[61] D.-Q. To, *Advanced kp multiband methods for semiconductor-based spinorbitronics*, Ph.D. thesis, Institut polytechnique de Paris (2019).

[62] T. H. Dang, Q. Barbedienne, D. Q. To, E. Rongione, N. Reyren, F. Godel, S. Collin, J. M. George, and H. Jaffrès, Anomalous hall effect in $3d/5d$ multilayers mediated by interface scattering and nonlocal spin conductivity, Phys. Rev. B **102**, 144405 (2020).

[63] D. Q. To, T. H. Dang, L. Vila, J. P. Attané, M. Bibes, and H. Jaffrès, Spin to charge conversion at rashba-split **srtio**$_3$ interfaces from resonant tunneling, Phys. Rev. Research **3**, 043170 (2021).

[64] A. Woessner, M. B. Lundeberg, Y. Gao, A. Principi, P. Alonso-González, M. Carrega, K. Watanabe, T. Taniguchi, G. Vignale, M. Polini, *et al.*, Highly confined low-loss plasmons in graphene–boron nitride heterostructures, Nature materials **14**, 421 (2015).

[65] A. Kumar, T. Low, K. H. Fung, P. Avouris, and N. X. Fang, Tunable light–matter interaction and the role of hyperbolicity in graphene–hbn system, Nano letters **15**, 3172 (2015).

[66] F. J. Bezares, A. D. Sanctis, J. Saavedra, A. Woessner, P. Alonso-Gonzalez, I. Amenabar, J. Chen, T. H.

Bointon, S. Dai, M. M. Fogler, *et al.*, Intrinsic plasmon–phonon interactions in highly doped graphene: A near-field imaging study, Nano letters **17**, 5908 (2017).

[67] I. Epstein, D. Alcaraz, Z. Huang, V.-V. Pusapati, J.-P. Hugonin, A. Kumar, X. M. Deputy, T. Khodkov, T. G. Rappoport, J.-Y. Hong, *et al.*, Far-field excitation of single graphene plasmon cavities with ultracompressed mode volumes, Science **368**, 1219 (2020).

[68] L. Szunyogh, B. Lazarovits, L. Udvardi, J. Jackson, and U. Nowak, Giant magnetic anisotropy of the bulk antiferromagnets irmn and irmn$_3$ from first principles, Phys. Rev. B **79**, 020403 (2009).

[69] D. Wang, F. Tang, Y. Du, and X. Wan, First-principles study of the giant magnetic anisotropy energy in bulk na$_4$iro$_4$, Phys. Rev. B **96**, 205159 (2017).

[70] R. Albaridy, A. Manchon, and U. Schwingenschlögl, Tunable magnetic anisotropy in cr–trihalide janus monolayers, Journal of Physics: Condensed Matter **32**, 355702 (2020).

[71] K. Momma and F. Izumi, Vesta: a three-dimensional visualization system for electronic and structural analysis, Journal of Applied crystallography **41**, 653 (2008).

[72] Y. Li, Z. Jiang, J. Li, S. Xu, and W. Duan, Magnetic anisotropy of the two-dimensional ferromagnetic insulator mnbi$_2$te$_4$, Phys. Rev. B **100**, 134438 (2019).

[73] A. R. Wildes, D. Lançon, M. K. Chan, F. Weickert, N. Harrison, V. Simonet, M. E. Zhitomirsky, M. V. Gvozdikova, T. Ziman, and H. M. Rønnow, High field magnetization of feps$_3$, Phys. Rev. B **101**, 024415 (2020).

[74] S. M. Rezende, A. Azevedo, and R. L. Rodríguez-Suárez, Introduction to antiferromagnetic magnons, Journal of Applied Physics **126**, 151101 (2019).

[75] J. D. Jackson, *Classical electrodynamics, 3rd ed.* (Willey, New Jersey, 1999).

[76] A. Zangwill, *Modern Electrodynamics* (Cambridge University Press, Cambridge, 2012).